R. Barbieri, H. Montgomery, S. Qiu, B. Barnes, D. Knowles Jr., M. Che, and I.L. Goldberg, 1998: Draft of the MODIS Level 1B Algorithm Theoretical Basis Document Version 2.0 [ATBMOD-01], available from the NASA Goddard Spaceflight Center, Greenbelt Maryland.

S.F. Biggar, P.N. Slater, and D.I. Gellman, 1994: Uncertainties in the In-Flight Calibration of Sensors with Reference to Measured Ground Sites in the 0.4-11 μm Range, *Remote Sens. Environ.*, **48**, pp. 321-335.

R.M. du Plessis, 1967: Poor man's explanation of Kalman Filters or How I stopped worrying and learned to love matrix inversion, Rockwell International Technical Note, Anaheim, California.

E. Freedman and J. Byme, 1995: Combining Multiple Sources for Radiometric Calibration of LANDSAT 7 using a Kalman Filter, *Proc. IAPRS*, **30**, pp. 272-278.

A. Gelb (ed), 1974: *Applied Optimal Estimation*, MIT Press, Cambridge Mass., ISBN 0 262 70008-5.

H.H. Kieffer and R.L. Widley, 1992: Spectrophotometry of the Moon for Calibration of Spaceborne Imaging Instruments, in *Lunar and Planetary Science Conference* **23**, pp. 687-688.

H.H. Kieffer and R.L. Widley, 1996: Establishing the Moon as a Spectral Radiance Standard, *J. Atmos. Ocean. Tech.*, **13**, pp. 360-375.

P.N. Slater, S.F. Biggar, R.G. Holm, R.D. Jackson, Y. Mao, M.S. Moran, J.M. Palmer, and B. Yuan, 1987: Reflectance and Radiance Based Methods for the in-flight Absolute Calibration of Multispectral Sensors, *Remote Sens. Environ.*, **22**, pp. 11-37.

P.N. Slater and S.F. Biggar, 1996: Suggestions for Radiometric Calibration Coefficient Generation, *J. Atmos. Ocean. Tech.*, **13**, pp. 376-382.

P. Slater, B. Biggar, K. Thome, D. Gellman, and P. Spyvak, 1996: Vicarious Radiometric Calibrations of EOS Sensors, *J. Atmos. Ocean. Tech.*, **13**, pp. 349-359.

3. INTERBAND REGISTRATION

James Theiler and Barham W. Smith

3.1 Introduction and Goal

Registration is the process of overlaying multiple images of the same scene, so that a position in the scene corresponds to the same position in each of the images. Interband registration is crucial for virtually any kind of retrieval that depends on the spectral signature of the desired quantity; this includes vegetation, columnar water vapor, and surface water temperature. For the images produced by the Multispectral Thermal Imager (MTI), several registration steps will be required.

- Comparison with ground truth will require precise "geolocation," that is, direct registration of the images with absolute position on the ground.

- For an application such as change detection, it is necessary to register images of the same scene taken at different times.

- For a given overlook, the telescope will be maneuvered in orbit so that two separate views are obtained, one near nadir, and one at a shallower angle. Since the two looks are through different amounts of atmosphere, effects due to the atmosphere can be deduced (and corrected) independent of external climate or weather knowledge. The robust water temperature retrieval algorithm, for instance, is based on a linear fit to the TOA brightness temperatures in the thermal bands as seen from two distinct look angles. However, the perspective and field of view for the two looks will be quite different, and the registration of images from these two views will be a challenge.

- Swaths of the three sensor chip assemblies (SCA's) overlap by several pixels. This overlap region will be used to register the images generated by the individual SCA's.

- But a step that will precede all of these is the interband registration of images in each SCA. It is this initial step that is discussed here.

The MTI instrument is a push-broom scanner; each SCA in the focal plane consists of several (one for each spectral channel) single-pixel "stripes" of pixels that are scanned across the image (actually, the lines are two pixels wide, but only one of the two pixels will be collecting data on any given scene). The image is built up one row at a time as the SCA is pushed across the scene. The sampling interval in the cross-track direction is determined by the pixel spacing on the focal

plane, and the sampling interval in the along-track direction is determined by the ground-track speed and the pixel readout rate. For near nadir looks, the ground sample distances (GSD's) are approximately 20 meters in the thermal bands, and 5 meters in the VIS/NIR bands. The reconstruction of the scene requires that the motion of the imager be known very accurately; in particular, any jitter in the scanning motion will degrade the image. (Although the term "jitter" connotes high-frequency motion, we are using the term to mean any deviations from uniform scanning motion.)

3.2 Scientific Basis

If this jitter can be measured (for instance, with accurate on-board gyroscopes or accelerometers), then it can be accounted for in the image reconstruction; the problem basically reduces to an interpolation. However we expect that external jitter measurements will not be sufficiently precise, and we will need to infer information about motion of the FOV from the image data itself. This is the "analysis" block in the figure below.

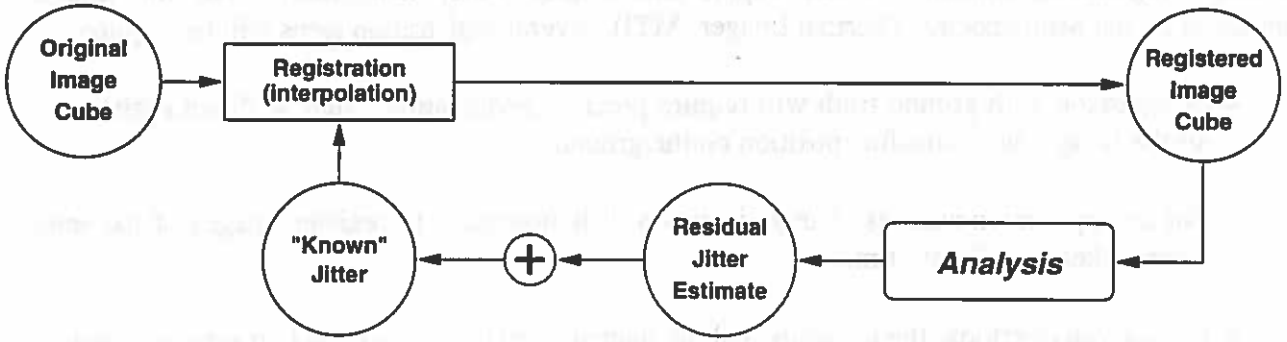

Figure 3-1. This figure emphasizes that registration requires jitter reconstruction and interpolation. The interpolation is always on the original datacube to prevent successive blurring.

For multichannel push-broom imagers, the individual stripes are physically separated on the focal plane so that each channel "sees" a particular part of the scene at a different time. Although this adds difficulty to the problem of registering the different channels to each other, it actually provides information that can be exploited in reconstructing the unknown jitter in the scanning motion, which can then be used for more accurate pixel registration and image reconstruction.

The basic idea is that there is cross-correlation between spectral channels. What's bright in the J band is generally bright in the K band. In particular, one can cross-correlate one stripe of band J with a stripe of band K at several different offsets, and take the offset that produced the maximum cross-correlation as the best guess for the offset.

3.3 Algorithm Steps

In Theiler *et al.*, 1997, we investigated two approaches based on cross-correlation for estimating both the along-track and cross-track jitter. The first approach involved cross-correlations between

each of the pairs of channels. The second method involved averaging all channels to make a "baseline" image, and then cross-correlating each channel to that baseline. Although less accurate than the pairwise method, the baseline approach is simpler and considerably faster. Finally, we investigated a variant of the baseline method that computed an iterative correction. Several iterations of this approach were found to produce results comparable in accuracy to (and still faster than) the pairwise method. Theoretical considerations (again, see Theiler *et al.*, 1997) suggest that the pairwise method is applicable over a wider range of conditions, but for the parameters of the MTI satellite and focal plane, the iterative baseline approach seems entirely adequate.

The pairwise algorithm involves generating a large, but highly structured matrix; in fact, it is banded, sparse, symmetric, positive semi-definite and approximately Toeplitz. This structure permits an accelerated iterative solution of a matrix equation, but it is still much slower than the baseline algorithm, which follows:

1) First, register the images in each channel as well as possible using nominal estimates of tracking velocity, possibly augmented by the jitter information from the onboard gyroscopes.
2) Create a baseline image by averaging the images in each channel.
3) Find the offset in both the along-track and cross-track directions that maximizes the cross-correlation between each channel and the baseline. This will produce a for each band an estimate of the jitter as a function of time.
4) Average these individual estimates of jitter to get an overall estimate of the jitter.
5) Add this residual jitter to the nominal jitter in step 1 to obtain a refined estimate of the jitter.
6) Use interpolation to actually register the images.

The iterative baseline algorithm is a straightforward enhancement. The idea is to re-use the estimated jitter from step 5 as the "nominal" jitter in step 1. The registration in step 1 is always performed on the original image cube, so there is no successive blurring of the image cube. Steps 1 through 5 can be repeated until the residual jitter in step 4 is sufficiently small. Step 6 is only performed once, at the very end, to obtain a registered image. However, as we have noted, interband registration is just one of a series of registration steps that will need to be performed. To avoid successive blurring effects, we will not use registered images as intermediate data products, between the different registration steps. The most important data product for the interband registration is the estimate of jitter as a function of time.

3.4 Error Budget

Simulations (shown in Figures 3-2 and 3-3; see Theiler *et al.*, 1997, for details) suggest that the registration error can be made well below one pixel.

3.5 Validation

The registration algorithm can in principle be applied to any subset of spectral bands, though there is a qualitative difference between the visible bands and the thermal bands. The visible bands have

smaller pixels, but the thermal bands have more band-to-band correlation.

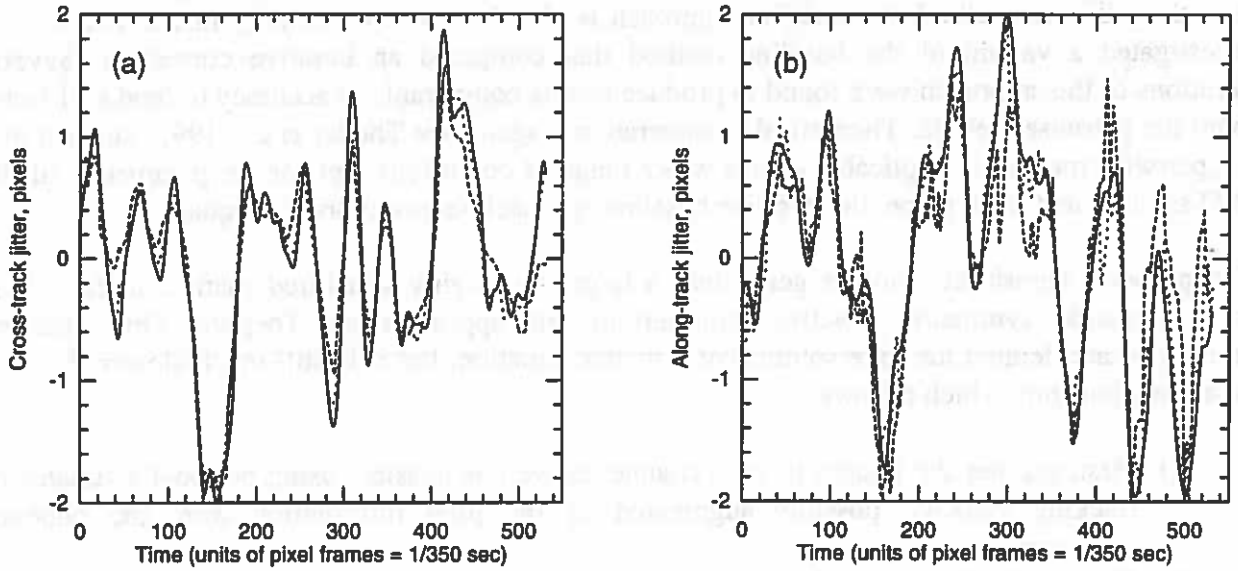

Figure 3-2. Simulated jitter in the cross-track and along-track directions is estimated using both the pairwise and the baseline algorithm. For this particular simulation, the cross-track rms errors were 0.162 pixels (pairwise) and 0.276 pixels (baseline). The along-track rms errors were 0.226 pixels (pairwise) and 0.475 pixels (baseline). Along-track jitter estimation is in general less accurate than cross-track estimation.

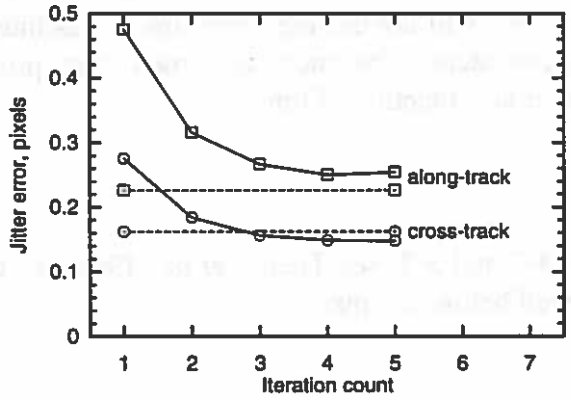

Figure 3-3. Iterating the baseline jitter estimation algorithm provides a considerable improvement. In particular, the iterated baseline algorithm is comparable in accuracy to the more expensive pairwise algorithm.

Application of the algorithm separately to the visible bands and to the thermal bands will produce two separate jitter estimates; the extent to which these estimates agree provides an indirect measure of registration accuracy that can be performed without any ground truth.

Though the algorithm does not depend on particular features in the ground, some features can be very helpful in assessing the accuracy to which the registration is performed. Scenes with long straight lines are particularly useful in this regard: roads, channels, runways, parking lots, and city blocks are among the features for which "straightness" on the registered image can be assessed. Further assessment can be done if accurate maps of these features are available.

Another validation approach requires more active ground efforts. Isolated high-contrast GPS-located targets can test not only the interband registration, but also the two look registration, and even the full-up geolocation. At least two experiments of this kind should be performed, one on flat terrain, and one where topography is a more serious consideration. One way to make the target is to have a 20 meter square tarp (black, say) inside a 60 meter square tarp of contrasting color. (The background tarp may not be necessary if the background seen is sufficiently uniform; eg, a dry lake bed.) Because the inner tarp just fits into a pixel, it will generally map into four adjacent pixels. But because the background is uniform, one can linearly decompose the amount of the image that is in each pixel and locate it to a precision that is much less than the size of a pixel. Because these are rather large tarps, an alternative approach would be to set up much smaller mirrors which are aimed to reflect sunlight specularly into the satellite. If the reflected sunlight is too bright, then it will affect the registration algorithm (will probably help it) in a way that does not represent the behavior of the algorithm on typical scenes.

3.6 Software Implementation Concept

The software for both algorithms has been implemented in IDL and is part of the MTI Software Repository. We would like to acknowledge the contributions of Bradley G. Henderson. Software for the registration of the SCA's to each other, and for registration of the two looks to each other, has not been developed. The focal plane distortion map also remains to be integrated into this task. This software will probably be based on standard techniques, such as those reviewed by Fonesca *et al.*, 1996. We note that this integration will require that jitter information be carried along with the data. The actual interpolation will always be saved for last, avoiding unwarranted blurring in the final image cube due to re-registration at intermediate stages.

References

Borel, C. and D. Schläpfer, 1996a: "Atmospheric pre-corrected differential absorption techniques to retrieve columnar water vapor: theory and simulations," in *Proceedings of the 6th JPL Airborne Earth Science Workshop (AVIRIS '96).*

Borel, C., W. B. Clodius, and J. Johnson, 1996b: "Water vapor retrieval over many surface types," in *Algorithms for Multispectral and Hyperspectral Imagery II*, A. Iverson, ed., *Proc. SPIE*, **2758**, pp. 218-228.

Carper, T. W., T. M. Lillesand, and R. W. Kiefer, 1990: "The use of intensity-hue-saturation transformation for merging panchromatic and multispectral image data," *Photogrammetric Engineering and Remote Sensing*, **56**, pp. 459-467.

Chan, C. L., *et al.*, 1996: "Performance of an adaptive algorithm for suppressing intraframe jitter in a 3-D signal processor," in *Signal and Data Processing of Small Targets 1996*, O.E.Drummond, ed., *Proc. SPIE*, **2759**, pp. 42-61.

Fonesca, L. M. G. and B. S. Manjunath, 1996: "Registration techniques for multisensor remotely sensed imagery," *Photogrammetric Engineering and Remote Sensing*, **62**, pp. 1049-1056.

Henderson, B. G., C. C. Borel, J. Theiler, and B. W. Smith, 1996: "Image quality degradation and retrieval errors introduced by registration and interpolation of multispectral digital images," in *Signal and Data Processing of Small Targets 1996*, O.E.Drummond, ed., *Proc. SPIE*, **2759**, pp. 149-160.

Piotrowski, C. C., M. S. Farber, S. J. Hemple, and W. S. Helliwell, 1996: "An analysis of advantages and disadvantages of scene registration as a part of space-time processing," in *Signal and Data Processing of Small Targets 1996*, O.E.Drummond, ed., *Proc. SPIE*, **2759**, pp. 98-110.

Theiler, J., B. G. Henderson, and B. W. Smith, 1997: "Algorithms Using Inter-band Cross-correlation for Pixel Registration and Jitter Reconstruction in Multichannel Push-broom Imagers," *Proc. SPIE*, **3163**, pp. 22-32.

Tornow, C., C. C. Borel, and B. J. Powers, 1994: "Robust water temperature retrieval using multispectral and multi-angular IR measurements," *Proc. IGARRS '94*, pp. 441-443.

4. IMAGE RECONSTRUCTION AND RESTORATION

Christoph C. Borel

4.1 Introduction and Goal

The purpose of image restoration is to correct the measured image for degrading effects resulting from image blurring and additive noise. The blurring can be due to atmospheric turbulence, scattering caused adjacency blurring, telescope point spread function, motion and jitter during image acquisition, amplifier transfer function, electronic cross talk. The noise can be due to thermal noise (Gaussian), photon or shot noise (Poisson), correlated noise (1/f noise), read-out noise and quantization noise.

Image restoration will be used in MTI to improve water temperature estimates in the mid and long-wave channels and improve material identification accuracy in the visible, near and short-wave infrared. Image reconstruction attempts to improve the radiometric accuracy of the original data using knowledge about the blurring process and noise. In some cases a visible channel can be used to outline the water bodies and sharpen the images.

In summary the goals are to find methods to:

- Improve the image quality;
- Improve retrieved physical parameters such as water temperature;
- Improve material identification accuracy in the visible, near and short-wave infrared.

4. 1. 1 Image Reconstruction

We will not talk much about image reconstruction here and only state what additional steps are involved. In the context of MTI, image reconstruction is the step which takes individual image rows and places them such that they correspond to the 2-D scene observed by the telescope. To use an analog from art preservation, reconstruction takes the broken pieces of a vase and glues them together. Its algorithms are described in detail in the registration write-up and the write-up on geolocation.

However note that there will be residual blurring effects introduced by the interpolation step which depend on the interpolator used (e.g. nearest neighbor, bi-linear, bi-cubic, quintic). Therefore it is recommended to first perform an image restoration followed by the steps of image reconstruction.

4. 1. 2 Image Restoration

Using an analog from art preservation, restoration takes off the dark varnish layers of a painting and fills in cracks. A brief synopsis on image restoration can be found at:

http://web.eecs.nwu.edu/EXTERNAL/ivpl/other_rest.html

Restoration of single channel images is a relatively mature field, started back in the early 1970's, when digital computers were first making headway into the research laboratories across the country. Since the publication of *Digital Image Restoration* by Andrews and Hunt in 1977, restoration has been widely researched. The basic model for imaging is given by:

$$D = I * PSF + N \tag{4-1}$$

where D is the observed (data) and I the original image, N is the additive random noise (i.e. Gaussian or Poisson distributed), and PSF is the Point Spread Function. The discrete convolution is defined as (Városi):

$$(I * PSF)(i, j) = \sum_{k,l} I(k, l)PSF(i - k, j - l) \tag{4-2}$$

where (i,j) are image pixel indices and PSF is assumed to be centered at (0,0).

The problem of image restoration or deconvolution can now be mathematically stated as: Given D, find a best estimate of I, according to some optimization criterion. Restoration algorithms differ with respect to the amount of knowledge that is assumed known a priori . The simplest algorithms assume PSF is known exactly, as well as the statistics of the noise, N. Under this condition inverse filtering is a viable solution. However, in practice the degradation is often not well known, although it can be estimated by a couple of different methods. For example, if the image is an astronomical image, then the blur can be calculated by pointing the telescope at a star (point source). The observed image will not be a point, due to the degradation. Instead, the point will be blurry, which can then be used to estimate the degradation. In more general cases, different algorithms have been proposed in the literature to estimate the Point Spread Function.

4.2 Scientific Basis

Városi and Landsman (1995) state:

"The objective of deconvolution is to reconstruct the image I given the data D, the PSF, and knowledge of the noise N. In reality the image restoration problem has more unknown than known quantities because of noise and instrument limitations. For this reason a unique solution does not exist, so it is necessary to consider the probabilities of solutions. The statistical formulation of the deconvolution problem involves the use of Bayes' theorem to derive (see, e.g., Weir 1991, PiÒa and Puetter 1992)

$$p(I|D,M) = \frac{p(D|I,M)p(I|M)}{p(D|M)} \tag{4-3}$$

where $p(I|D,M)$ is the probability of the restored image given the data and model M (e.g. eq. 1) $p(D|I,M)$ is the probability of the data for a given restored image and model. Assuming the model is fixed, the term $p(D|M)$ is independent of I so it is constant, and $p(I|M)$ is the prior probability of the image given the model. A solution to the deconvolution problem is obtained by maximizing the probability of the restored image, and this can be accomplished by maximizing $p(D|I,M)$, *the* 'goodness of fit', leading to 'maximum likelihood' methods. Also, the product $p(D|I,M)\ p(I|M)$ could be maximized, with $p(I|M) = e^S$ and $S \propto$ 'entropy' of I, then leading to 'maximum entropy' methods. Hence the Bayesian formulation leads to a variety of algorithms for image restoration, each having its own statistics measure to be optimized in order to reconstruct the image."

4.3 Algorithm Steps

4. 3. 1 Image sharpening for water temperature retrieval

A simulation package has been written (C. Borel) which computes the radiance images for all 5 thermal channels at the focal plane of size n_x in the across track direction and n_y pixels in the along-track direction.

1. Compute image of aperture ($I_{aperture}$) for a wavelength λ.
2. Compute telescope optical transfer function (OTF): $OTF_{telescope} = \mathrm{FFT}(I_{aperture})2$.
3. Compute image of pixel (I_{pix}) at 10 times the resolution.
4. Compute pixel OTF: $OTF_{pixel} = \mathrm{FFT}\ (I_{pix})$.
5. Compute motion path in units of pixels as sum of linear motion and jitter: $[x(t),y(t)] = [0.,t/T]$

+ $[x_{jitter}(t), y_{jitter}(t)]$, $t = 0,...,T$, where the jitter is computed using estimated power-spectra for x/y translations.

6. Compute Motion OTF: $OTF_{motion} = \mathrm{FFT}(\delta(x,y))$, where $\delta()$ is the delta function.

7. Compute telescope+motion+focal plane OTF : $OTF_{system} = OTF_{telescope}\, OTF_{pixel}\, OTF_{motion}$.

8. Compute scene image: $D_{10} = \mathrm{FFT}^{-1}[\mathrm{FFT}(B(\lambda,T(x,y)))OTF_{system}]$, where $T(x,y)$ is a simulated temperature distribution and $B()$ is the Planck function.

9. Re-sample filtered image to 50 μm pixels: $D_1 = |\mathrm{rebin}(D_{10}, n_x/10, n_y/10)|$, where rebin is an IDL® function to generate a new image by averaging 10 by 10 pixels.

10. Add noise: $D_{1R} = D_1 + N[\sigma = \mathrm{B}(\lambda_i, 273.15°\mathrm{K})/SNR]$, where SNR is the signal-to-noise ratio.

11. Compute PSF at a spacing of one pixel: $PSF = |\mathrm{rebin}[\mathrm{FFT}^{-1}(OTF_{system}), m_x/10, m_y/10]|$ and normalize: $PSF = PSF/\mathrm{total}(PSF)$, where m_x and m_y are the size of the oversampled PSF (typically $m_x = m_y = 150$).

12. Run Maximum Entropy filter N times using PSF as known point spread function (or other image restoration methods) to compute an estimate of the radiance $L_{est}(x,y)$ which minimizes the degradations (blurring and noise).

13. Convert the restored image to a brightness temperature map: $T\lambda(x,y) = B^{-1}(\lambda, L_{est}(x,y))$.

14. Compute the water temperature $Test$ with the robust linear fitting procedure (Tornow et al, 1994):

$$T_{est} = T_0 + \sum_{5} a_\lambda T_\lambda(nadir) + b_\lambda T_\lambda(60deg) \tag{4-4}$$

or with a physics-based retrieval method based on spectral smoothness (Borel, 1997).

15. Compute error statistics: $\varepsilon T = \sigma(T(x,y) - T_{est}(x,y))$.

4. 3. 2 Image restoration for correlated noise

In the case of correlated noise (1/f noise) we developed an iterative algorithm to suppress the correlated noise while preserving the scene information (Borel, Cooke and Laubscher, 1996). Correlated noise occurs in many imaging systems such as scanners and push-broom imagers. The sources of correlated noise can be from the detectors, pre-amplifiers and sampling circuits. Correlated noise appears as streaking along the scan direction of a scanner or in the along track direction of a push-broom imager. We have developed algorithms to simulate correlated noise and pre-filter to reduce the amount of streaking while not destroying the scene content.

The pre-filter in the Fourier domain consists of the product of two filters. One filter whitens the correlated noise spectrum, the other is a low-pass filter function e.g. Gaussian or Hanning window with variable width to block high frequency noise away from the origin of the Fourier Transform of the image data. We have optimized the filter parameters for various scenes and find improvements of the RMS error of the original minus the pre-filtered noisy image.

4. 3. 3 Image blurring due to adjacency effect

Although the adjacency effect can be considered a type of atmospheric correction, we include it here because compensation for it follows roughly the same methodology as previous deblurring effects.

In the visible and near infrared the atmosphere causes additional blurring due to scattering of light from adjacent surface elements into the line of sight. The amount of adjacency blurring depends on the aerosol loading of the atmosphere and the albedo bidirectional reflectance distribution function (BRDF) of the adjacent surface. We developed a method to estimate the adjacency effect using the extended radiosity method (Borel and Gerstl, 1992a, 1992b) taking the surface BRDF and height dependent aerosol scattering phase functions into account. The resulting cover dependent PSF's can be used to realistically simulate top of the atmosphere radiances for artificial scenes.

When images of heterogeneous land surfaces are acquired through the atmosphere, the measured radiance data include not only the surface radiances per pixel but also contain modifications due to the atmosphere. Correcting such modified land imagery for atmospheric effects, one must consider atmospheric absorption as well as scattering. The atmospheric scattering gives rise to a blurring effect of adjacent pixels. The adjacency-blurring-effect is most noticeably observed at the boundary between a dark and a bright surface. Near the edge over a dark surface photons from the nearby bright surface may be scattered within the atmosphere into the field of view (FOV) of an airborne or satellite sensor. Conversely, near the edge over a bright surface fewer photons reach the sensor's FOV. At a discontinuity in the surface reflectance, the intensity transect in a satellite image appears therefore as the sum of a step and a sigmoid-shaped function. This blurring effect is most often observed at boundaries between surfaces with a large contrast ratio such as water and land in the visible, and has been described in the literature by Diner (1985), Kaufman (1984), Richter (1990), Pearce (1977), Tanré (1980) and others.

The adjacency-blurring-effect may introduce errors in the classification of small bright areas surrounded by a dark region, or dark areas on a bright background (Kaufman (1984)).

It is difficult to correct for the adjacency effect in practice but we hope to measure and document the effect with MTI data. There is also a potential to use the adjacency PSF as a way to characterize the aerosol parameters given a known ground reflectance field.

4. 3. 4 Image blurring in the visible, near and short-wave infrared due to cirrus clouds

Since cirrus clouds scatter in the visible, near and short-wave infrared image blurring will occur. It is not certain how imagery with cirrus clouds present can be sharpened. Discussions with Bo-Cai Gao indicate that it might be possible to use the cirrus channel at 1.37 μm to estimate the scattering in other channels and then correct for it. No attempts have been made to calculate the PSF of cirrus

for image sharpening of cirrus contaminated scenes. See Section 12 for more information on cirrus and Section 13 for aerosol correction.

4. 3. 5 Image blurring in the thermal infrared due to cirrus clouds

If thin cirrus are present the blurring in the thermal could be significant and we need to further investigate how much blurring results and to develop methods to correct the blurring from cirrus.

4. 3. 6 Blurring due to atmospheric turbulence

The blurring due to atmospheric turbulence has been estimated to be not important at the 5 m and 20 m GSD.

4. 3. 7 Veiling glare correction

A fraction of the light observed at the focal plane is due to scattered light from outside of the field of view. Bright objects like clouds could cause an additional radiance offset in each channel which would not be corrected by atmospheric corrections and basic image restoration methods. Using con-temporal imagery from a weather satellite (e.g. Goes, Meteosat) and laboratory data for the veiling glare it should be possible to estimate a radiance offset due to veiling glare for MTI imagery.

4.4 Error Budget

4. 4. 1 Water temperature error estimates

The error resulting from using various image restoration methods has been computed in the case of water temperature retrievals for various artificial scenes. The error depends on the scene complexity. For scenes with large uniform water bodies there are almost no improvements visible between unrestored and restored temperature maps. For high-temperature gradients and highly structured scenes there is a substantial improvement - often a factor of two - when an image restoration algorithm is used. A detailed error budget can be worked out on a case-by-case basis for MTI imagery using the algorithms out-lined above.

4. 4. 2 Material identification improvement estimates

Not done for MTI. Work by Gray (1986) indicates an improvement in classification accuracy.

4.5 Validation Plan

The image restoration algorithms can be validated using two sources of data from the sensor:

- The ground measurements using artificial targets projected into the MTI telescope together with detailed measurements of the modulation transfer function (MTF).
- Space-based measurements by MTI over resolution targets and of bright stars.

- Space-based measurements by MTI over targets with known reflectances and fractions to test material identification.

4.6 Software Implementation Concept

The following image restoration methods have been implemented:

- Maximum Entropy (Városi)
- Maximum Likelihood (Városi)
- Maximum Residual Likelihood (Városi)
- Goodness of Fit (Puetter)
- Weighted Goodness of Fit (Puetter)
- Pixon (Puetter)
- Iterative Wiener Filtering (Borel)

As an example, iterative Wiener filtering is an algorithm that works quickly and well to improve the water temperature retrieval. The steps for this algorithm are:

1. $f_0 = \omega D$
2. $f_k = f_{k-1} + \omega (D - f_k * PSF), \quad k = 1,...,N$

where f_k are the iterative estimates of the original image I and ω (> 0) is selected so that

$|1 - \omega MTF| < 1$.

References

Andrews H.C. and B. R. Hunt, 1977: *Digital Image Restoration*, Englewood Cliffs, NJ: Prentice-Hall.

Borel C.C. and S.A.W. Gerstl, 1992a: "Adjacency-Blurring-Effect of Scenes Modeled by the Radiosity Method," *Proc. SPIE'92*, Orlando, FL, pp. 620-624 and LA-UR-92-985.

Borel C.C. and S.A.W. Gerstl, 1992b: "Atmospheric Corrections using the Volume Radiosity Method", *Proc. of IGARSS'92*, Houston, TX, p.1231-1234 and LA-UR-92-709.

Borel, C.C., B.J. Cooke and B.E. Laubscher, 1996: "Partial removal of correlated noise in thermal imagery," *Proc. SPIE, AeroSense'96*, **2759**, pp.131-138.

Borel, C.C. 1997: "Iterative Retrieval of Surface Emissivity and Temperature for a Hyperspectral Sensor," in *Proceedings of the First JPL Workshop on Remote Sensing of Land Surface Emissivity*, NASA/Jet Propulsion Laboratory, Pasadena, Ca.

Diner D.J. and J.V Martonchik, 1985: "Atmospheric transmittance from spacecraft using multiple view angle imagery," *Applied Optics*, **24:21**, pp.3503-3511.

Gray, M.H. 1986: "Radiometric Correction of Satellite Imagery for Topographic and Atmospheric Effects," M.Sc. Thesis, Faculty of Forestry, Univ. of British Columbia, Vancouver, BC.

Kaufman Y.J., 1984: "Atmospheric effects on remote sensing of surface reflectance," *Proc. SPIE*, **475**, pp. 20-33.

Lim, 1990: *Two-dimensional Signal and Image Processing*, Prentice Hall, p.552.

Pearce W.A., 1977: "A study of the effects of the atmosphere on Thematic Mapper observations," Report 004-77, EG&G, Washington Anal. Serv. Center, Riverdale, MD.

Piña, R. K. and Puetter, R. C., ftp://cassir.UCSD.EDU/receive/imrecon.

Richter R., 1990: "A fast atmospheric correction algorithm applied to Landsat TM images," *Int. J. Remote Sensing*, **11**, pp.159-166.

Tanré D., M. Herman and P.Y. Deschamps, 1981: "Influence of the background contribution upon space measurements of ground reflectance," *Applied Optics*, **20:20**, pp.3676-3684.

Tornow C., private communication.

Városi F., and W. B. Landsman, "An IDL Based Image Deconvolution Software Package," Hughes STX Co., Code 685, NASA/GSFC, Greenbelt, MD 20771; see also ftp://idlastro.gsfc.nasa.gov/contrib/varosi.

Weir, N., 1991: in *Proceedings of the 3rd ESO/ST-ECF Data Analysis Workshop.*

5. PHYSICS-BASED WATER AND LAND TEMPERATURE RETRIEVAL

Christoph C. Borel and John J. Szymanski

5.1 Introduction and Goal

Currently we have a well-documented and robust algorithm to retrieve water temperatures (see Section 6). The robust algorithm uses a linear fit to measured top-of-the-atmosphere (TOA) brightness temperatures for nadir and off-nadir (60 degrees) looks. Unfortunately the algorithm is complex to use since a large set of atmospheric cases must be run to come up with the linear fitting coefficients. The robust water temperature algorithm is also not able currently to retrieve land surface temperatures, since it does not explicitly include the surface emissivity, although it could be modified to do so.

Thus we decided to work on a new algorithm to retrieve not only water temperatures but also land surface temperatures. Recently we presented work on an algorithm to retrieve surface temperature and emissivity for a hyper-spectral imager in the long-wave infrared (see C. Borel, 1997). We found that we could apply the main idea of the algorithm to the multi-spectral case as well. Having a physics-based algorithm will provide us with another method which can be compared to the robust water temperature retrievals.

5.2 Scientific Basis

5. 2. 1 Water surface temperature retrieval

The central problem of temperature-emissivity separation is, as pointed out by Realmuto, 1990, that we obtain N spectral measurements of radiance and need to find N+1 unknowns (N emissivities and one temperature). To solve this problem in the presence of the atmosphere we need to find even more unknowns: N spectral transmissions $\tau_{atmo}(\lambda)$, N up-welling path radiances $L_{path}\uparrow(\lambda)$ and N down-welling path radiances $L_{path}\downarrow(\lambda)$. Fortunately there are radiative transfer codes such as MODTRAN 3 and FASCODE available to get good estimates of $\tau_{atmo}(\lambda)$, $L_{path}\uparrow(\lambda)$ and $L_{path}\downarrow(\lambda)$ on the order of a few percent.

The presently-used methods for multi-spectral sensors such as TIMS, ASTER, etc. are based on assumptions of having a certain emissivity ε_i at a wavelength λ_i (Kahle et al., 1980), fixing the maximum expected emissivity to a certain value (Realmuto, 1990), assuming a linear relationship between mean emissivity and maximum difference for

rocks and soils (Matsunaga, 1993) and approximating the Planck function using Wien's law and working with residuals (temperature and alpha) (Hook et al, 1992).

Our algorithm varies the columnar water vapor and atmospheric temperature over a small range of surface temperatures until the retrieved surface temperature is the same for all spectral channels while matching the measured radiances. We found that while the atmospheric temperature and columnar water vapor may be in error to actual values used in MODTRAN the retrieved surface temperature is actually very close to the truth. Thus the method should not be used to retrieve atmospheric parameters.

The algorithm was tested on synthetic data using spline fits to many MODTRAN runs and a independently-derived nonlinear model for the atmospheric transmission based on work by J. Johnson and W. Clodius, 1995. For now we use a simple emissivity model for water.

5. 2. 2 Land surface temperature retrieval

The above algorithm has not been tested yet for land surfaces. We imagine that it will be necessary to combine a material identification algorithm using the NIR and SWIR channels and estimate the material emissivity in the thermal channels and then run the same algorithm to determine water temperatures with a new emissivity.

Alternatively we will compare our algorithm to TES algorithms used for ASTER.

5.3 Algorithm Steps

The main idea is that the atmospherically-corrected surface temperature should be the same in all MTI thermal channels. The measured radiance for channel i is given as:

$$L_{m,i} = \varepsilon_{g,i} B_i(T_g) T_i(CW) + B_i(T_a)[1 - T_i(CW)] \quad (5\text{-}1)$$

where ε_g is the ground emissivity, $B_i(T_g)$ is the band-averaged Planck function for band i with the subscripts g indicating ground and a indicating the atmosphere. The columnar-water-vapor dependent transmission is written as $T_i(CW)$.

Solving eq.(5-1) for the estimated ground temperature $\langle T_{g,i} \rangle$ for the i-th channel:

$$\hat{T}_{g,i} = B^{-1}\left[\frac{l_{m,i} - B_i(T_a)(1 - T_i(CW))}{\varepsilon_{g,i} T_i(CW)}\right] \quad (5\text{-}2)$$

where $B^{-1}[]$ indicates the inverse band-averaged Planck function. Known quantities are the measured radiance at the sensor $L_{m,i}$ and the surface emissivity $\varepsilon_{s,i}$; the unknowns are the effective atmospheric temperature T_a and the columnar water vapor CW.

We found (J. Johnson and W. Clodius, 1995) that the following equation is a very good approximation for the band-averaged atmospheric transmission $T_i(CW)$:

$$T_i(CW) = \exp\left[-\left(\frac{A_i}{\cos\theta} + B_i\left(\frac{CW}{\cos\theta}\right)^{C_i}\right)\right] \tag{5-3}$$

where A_i, B_i and C_i are fitting parameters obtained by varying the columnar water vapor for nadir $\theta = 0°$ and off-nadir $\theta = 60°$ looks.

Table 1: Fitting Coefficients

Channel i	A_i	B_I	C_i
J	0.0753401	0.0691721	0.855049
K	0.0418199	0.778816	0.666231
L	0.121604	0.304723	0.768838
M	0.0479972	0.158434	0.836417
N	0.0223214	0.0731050	1.39088

The algorithm consists of varying the columnar water vapor and atmospheric temperature over a small range of surface temperatures until the retrieved surface temperature $\hat{T}_s$ is the same for all spectral channels *i*, while matching the measured radiances $L_{m,i}$.

5.4 Error Budget

Needs to worked out in detail - indications are that the temperature accuracy is very good (i.e., < 1K for most atmospheric cases).

5.5 Validation Plan

See Section 6, following.

5.6 Software Implementation Concept

Simulation program exists called smoothall.pro which computes the temperature error as a function of water vapor and atmospheric temperature.

References

Borel, C.C. 1997: "Iterative Retrieval of Surface Emissivity and Temperature for a Hyperspectral Sensor," in the proceedings of the *First JPL Workshop on Remote Sensing of Land Surface Emissivity.*

Hook S.J., A.R. Gabell, A.A. Green and P.S. Kealy, 1992: "A comparison of techniques for extracting emissivity information from thermal infrared data for geologic studies," *Remote Sens. Environ.*, **42**, 123-135.

Kahle, A.B., D.P. Madura and J.M. Soha, 1980: "Middle infrared multi-spectral aircraft scanner data: analysis for geologic applications," *Applied Optics*, **19(14)**:2279-2290.

Matsunaga, T., 1993: "An emissivity-temperature separation technique based on an empirical relationship between mean and range of spectral emissivity," *Proc. 14th Japanese Conf. of Remote Sensing*, 47-48.

Realmuto, V.J., 1990: "Separating the effects of temperature and emissivity: emissivity spectrum normalization," Proc. of the Second TIMS Workshop, *JPL Publ.* **90-55**, 31-35.

Salisbury, J. W. and D. M. D'Aria, 1992: "Emissivity of terrestrial materials in the 8-14 μm atmospheric window," *Remote Sens. Environ.*, **42**, 83-106.

6. ROBUST WATER TEMPERATURE RETRIEVAL

James Theiler, Christoph C. Borel, and Pawel Smolarkiewicz

6.1 Introduction and Goal

Temperature retrievals over water surfaces are simplified by the near-blackbody radiance of water in the thermal IR bands, but complicated by atmospheric conditions (water vapor, cirrus clouds, aerosols, *etc.*) through which the surface is viewed. In the absence of atmospheric effects, one could compute water temperature using any one of the MTI thermal channels (J,K,L,M,N), and the algorithm would have only two steps:

1. Divide radiance by known emissivity of water in the desired waveband;

2. Convert this radiance to temperature using the Planck blackbody formula.

If the atmospheric conditions are known, their effects can be modeled, (*e.g.*, with MODTRAN (Berk, 1989)), and a corrected estimate of water surface temperature is possible, again from any one of the MTI thermal IR channels. The "robust" water temperature retrieval algorithm does not assume that atmospheric conditions are known, but it takes advantage of the fact that radiances are measured in five different spectral bands; it also exploits the two looks that the MTI satellite makes in a given pass over a target. The algorithm used for MTI is a variant of Barton's method (Barton 1989) developed by Tornow *et al.* (Tornow and Borel 1994, and Tornow *et al.* 1994). It estimates the water surface temperature without using external information about the atmosphere, and (in simulations) it provides a reasonably accurate approximation over a wide variety of atmospheric conditions.

6.2 Scientific Basis

Figure 6-1 identifies three components contributing to the TOA radiance which is finally measured by the satellite. Since the atmospheric effects are different in different spectral channels, and vary with the amount of atmosphere through which the scene is being viewed, it is in principle possible to infer information about the atmosphere from the collection of individual measurements of TOA brightness temperature in the different thermal channels and different look angles. It is difficult to directly infer atmospheric properties from these variations, but the "robust" approach sidesteps this difficulty by combining these individual measurements to provide an estimate which is relatively insensitive to atmospheric variations. The final estimate

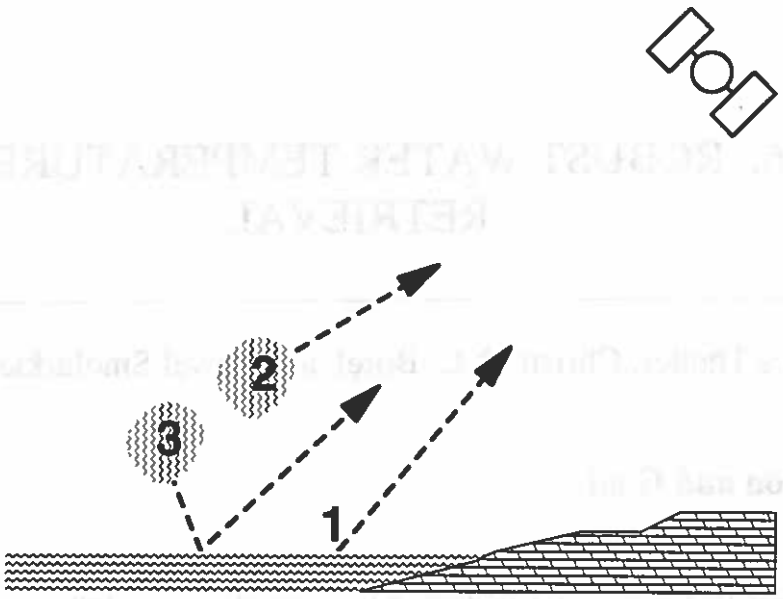

FIGURE 6-1. Three components are identified as contributing to the TOA radiance. 1) is the radiance from the surface; this the quantity we most care about since it contains information about the surface temperature. 2) is upwelling radiation from the atmosphere, and 3) is reflected downwelling radiation. All three of these contributions are attenuated by the atmsophere.

is the linear combination of the individual TOA brightness temperature measurements that best fits the actual surface temperature over a variety of atmospheric conditions. The front-end of the approach is to model the radiation transport through a variety of atmospheres. For each channel, and for each of two look angles, the TOA brightness temperature is computed as a function of surface water temperature. These functions, one for each atmospheric model and look angle, constitute a "database" of surface temperatures and corresponding TOA brightness temperature measurements.

Note that we assume a plane parallel atmosphere, in which the viewing paths through both look angles pass through the same atmospheric structure at different angles. In the daytime, MTI can check this assumption by direct measurement of the water vapor column along each path, since the variability of water vapor is the major factor in variability of path radiance and absorption. At night, however, we have no check.

A sticky point here is the combinatorial explosion of possible models to run. One wants the database to span a range of water vapor levels, aerosol quantities, and aerosol types, to include various thicknesses of cirrus clouds, and to cover an adequate range of ground temperatures. In Tornow and Borel (1994), an approximation is described for obtaining TOA radiances as a function of ground surface temperature, given a model prediction at a fiducial ground surface temperature. The basic idea involves defining an "effective transmittance" for a given spectral channel which depends very weakly on ground temperature, and then approximating it by its value at the fiducial temperature. Since the only other temperature dependence in the model comes from the black-body radiance, this can be calculated after the MODTRAN runs. Thus, only one MODTRAN run is needed for each atmospheric model. Given the possible

combinations of water vapors, aerosols, *etc.*, this can still be quite large, but this approximation reduces the job from tens of thousands of runs to a few hundred. This a large number of MODTRAN runs, but fortunately it is not necessary to make a separate run for each ground temperature.

The back-end of this method attempts to invert the model by linear regression of the water surface temperatures to the corresponding TOA brightness temperatures.

Although water is a near-blackbody (in other words, emissivity is near one) in the thermal regime, the robust water temperature retrieval algorithm only depends on the fact that its emissivity is known. Land temperature retrieval can use the same robust algorithm as long as the emissivity of the ground can be determined or estimated. This may be possible by using other bands for material identification, and then using a database of material spectral properties in the infrared.

6.3 Algorithm Steps

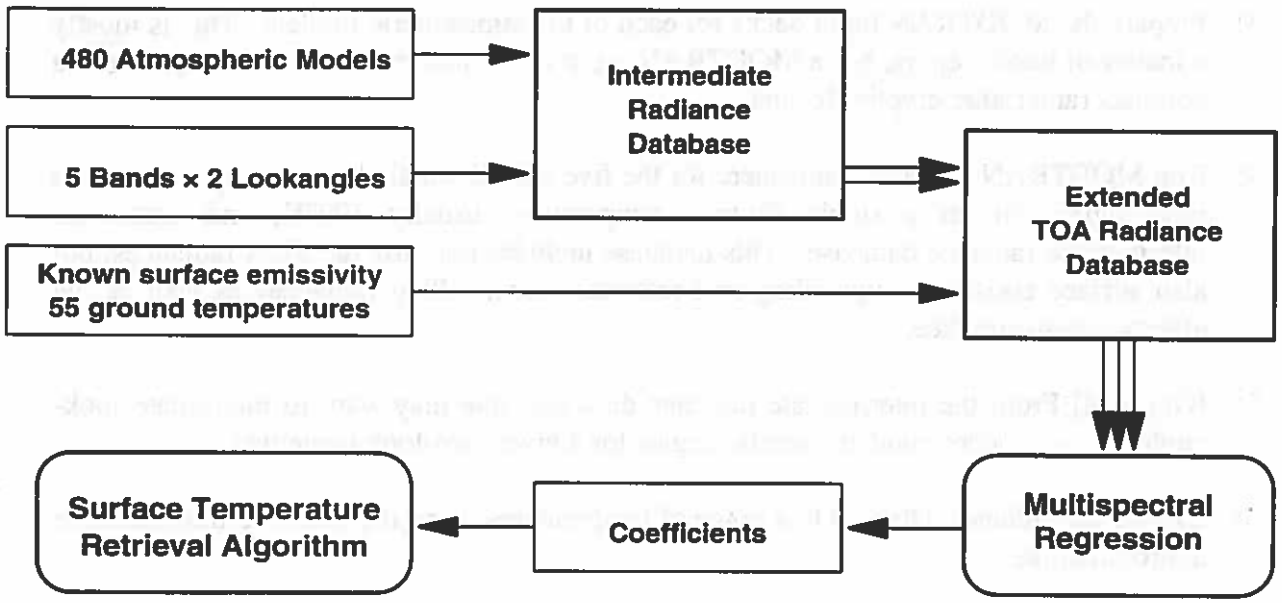

Figure 6-2. Database approach to temperature retrieval. The intermediate radiance database contains information on atmospheric transmission, upwelling radiance, and reflected downwelling radiance for a wide range of atmospheric conditions, as seen in the five thermal bands at two different lookangles. Generating the intermediate database involves a large number of MODTRAN runs. From these intermediate values, the final TOA radiance for a given ground emissivity and and ground temperature can be quickly computed (without recourse to MODTRAN). An extended radiance database can then be built with TOA radiances (or, equivalently, TOA brightness temperatures) in each of the ten band/angle combinations over a wide range of ground temperatures. Using linear regression, coefficients are found which optimally fit the ground temperature as a function of TOA brightness temperatures. These coefficients comprise the robust water temperature retrieval algorithm.

The retrieval algorithm itself is actually quite trivial, it is a set of coefficients which are applied to the TOA brightness temperatures to produce an estimated ground temperature. To obtain these coefficients, we use a database approach as shown in Figure 6-1. The algorithm is explained in more detail in Tornow and Borel (1994), Tornow *et al.* (1994) and Theiler (1995), but an overall outline follows:

1) Choose a set of atmospheres to model. In the current implementation, these include twenty different water vapor levels, varying from a sub-arctic 0.09 g/cm^2 to a tropical 4.2g/cm^2; three types of aerosol (urban, rural, and tropospheric); and eight atmospheric states (without and with volcanic aerosol, without and with varying thicknesses and altitudes of cirrus clouds). There are a total of 480 different atmospheres.

2) Compute (or look up) the emissivity of water; this value will depend on look-angle and on wind velocity, since wind roughens the surface. We use a Cox-Munk (Cox and Munk, 1954) model to estimate the effect of wind-roughening. See also Theiler and Henderson (1997), and Henderson *et al.* (1997).

3) Prepare the MODTRAN input decks for each of the atmospheric models. This is mostly a matter of bookkeeping, but a MODTRAN input deck contains a lot of information in a compact (and rather cryptic) format.

4) Run MODTRAN on each atmosphere for the five MTI thermal channels and at least two look-angles, but at a single fiducial temperature, usually 300°K, and create an intermediate radiance database. This database includes not only the TOA radiances, but also surface emissivity, upwelling and reflected downwelling radiances as well as the effective transmittance.

5) [Optional] From the intermediate radiance database, one may want to interpolate look-angles so as to accommodate specific angles for a given two-look maneuver.

6) Extend the radiance database to a range of temperatures using the effective-transmittance approximation.

7) Convert TOA radiance to TOA brightness temperature.

8) Perform the linear regression to invert the model.

One obtains from these steps a set of regression coefficients. These coefficients can then be used for conversion of TOA radiance measurements back to surface temperatures.

The typical data flow for this product is illustrated by Figure 6-3 for one- and two-look data analyses respectively. Algorithms implementing image enhanced water temperature retrievals will generate the data sets Level 2-WST-α-MEM and Level 2-WST-α-Pixon, which rely on Maximum Entropy and Pixon image enhancement techniques, respectively.

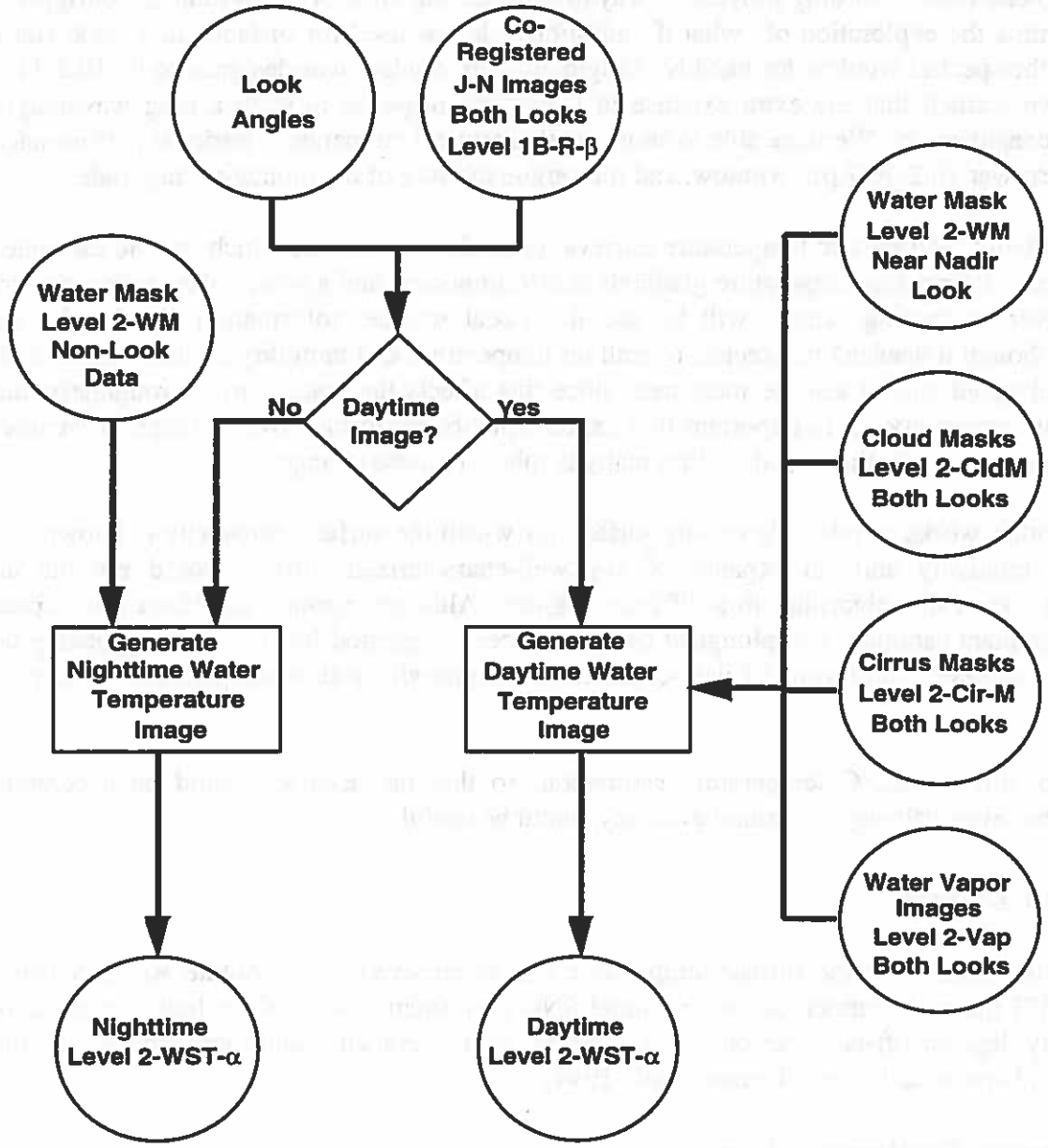

Figure 6-3. Water temperature retrieval data flow (two looks).

6.4 Validation Plan

In the end-to-end modeling, these retrieved surface temperatures are then compared to the temperatures used in the simulation, and this provides an estimate of the error due to modeling. The simulations also add noise (of two different kinds) in each of the spectral channels, and can

estimate the effect of signal to noise ratio in a given spectral channel on the final retrieved temperature.
The end-to-end model not only provides a way to estimate the error of the system as configured, it also permits the exploration of "what if" questions. It was used for instance in a trade study involving the spectral window for band N. Originally, this window was designed to be 10.2-11.5 μm, but we learned that the extra expense in taking the response to such a long wavelength would be considerable. We were able to show nearly identical temperature retrieval performance using a narrower 10.2-10.7 μm window, and thus argue in favor of the money-saving trade.

Direct validation will require temperature retrieval of a lake or pond for which ground estimates are available. Retrieving temperature gradients is also imporant, and a power plant with a nearby cooling river or cooling estuary will be useful. Local weather information should also be available, though it needen't be precise: overall air temperature and humidity are most important. Local wind speed should also be measured, since this affects the water surface roughness and therefore its emissivity. It is important that experiments be performed over a range of weather conditions to assess whether the algorithm really is robust to those changes.

This algorithm works in principle on any surface for which the surface emissivity is known. A large and relatively uniform expanse of any well-characterized surface would provide an interesting test of this algorithm in a different regime. Although parking lots, lava flows, coal fields, large plant canopies, and ploughed fields have been suggested for this, it will probably be difficult to achieve a uniform and well-characterized emissivity and/or temperature for any of these.

We would aim for 0.2°C temperature estimation, so that the accuracy could be accurately assessed, but even half-degree ground accuracy would be useful.

6.5 Error Budget

Simulations indicate that the surface temperature can be retrieved high absolute accuracy using the five MTI thermal channels at their nominal SNR performance, and taking both a nadir look and a sixty-degrees off-nadir second look. Again, more detailed results are reported in the references (Tornow and Borel, Tornow *et al.*, 1994).

6.6 Software Implementation

The MTI temperature retrieval algorithms are implemented with a combination of *perl* and *IDL* scripts which set up the input for and further process the output from a large *FORTRAN* routine (MODTRAN) that simulates atmospheric transmission of radiation. There is also a *Tk/Tcl* script (tktrp) which acts as a graphical front end to the entire pipeline. These are maintained in a software repository (see Theiler 1995). MODTRAN is the main workhorse of the temperature retrieval effort. The version we use has been modified so that it outputs not only the total top of atmosphere (TOA) radiance, but the contributions to that radiance due to surface emission, atmospheric upwelling emission, and reflected atmospheric downwelling emission. Using these

individual contributions permits us to extrapolate TOA radiance for a wide range of ground temperatures, from MODTRAN output computed with a single fiducial ground temperature.
The front-end of the pipeline involves generating a database of TOA radiances in our five thermal channels (J, K, L, M, and N) for a range of ground temperatures, a variety of atmospheric conditions, and for several different look angles.

The back-end attempts to "fit" this database to some kind of regression, providing coefficients for later use, and then quantifies the error between the fit and the database. We are interested not only in how well the fit matches the database, but also in how well a fit applied to noisy TOA radiances matches the database. Finally, the function `rad_to_temp` uses the coefficients generated in the back-end fit, and converts a set of TOA radiances into a best guess at the ground temperature.

We acknowledge the original work by Carmen Tornow to implement this algorithm.

Fig. 6-4 shows an overview of the main pipeline in its current implementation. More details can be found in the software write-up. (Theiler, 1995)

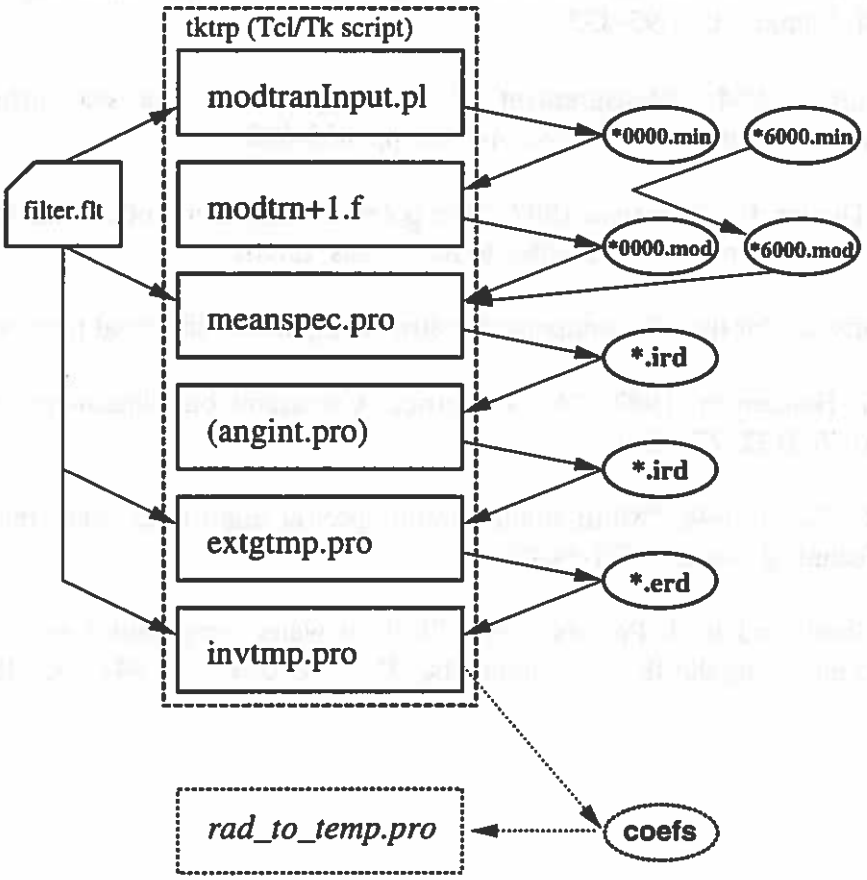

Figure 6-4: Temperature retrieval pipeline, in its current implementation. The `*.min` files are MODTRAN input decks (the filename encodes information about look angle and atmosphere type); the `*.mod` files are MODTRAN output. The `*.ird` file is an intermediate radiance

database, and the `*.erd` file is an extended radiance database. The `filter.flt` file contains information about the filter functions for the individual bands; in the production routine, this information will be managed by `*.pan` files. The six components in the front-end are run from a single Tcl/Tk script which provides a graphical user interface. The front-end of the pipeline produces the coefficients that are used in the back-end IDL script that converts TOA radiances to ground temperatures.

References

Barton, I. J., A. M. Zavody, D. M. O'Brien, D. R. Cutten, R. W. Saunders, and D.T. Llewellyn-Jones, 1989:*J. Geophys. Res.-Atmos.* **94**, 3365-3375 (1989).

Berk, A., L. S. Bernstein, and D. C. Robertson, 1989: "MODTRAN: A moderate resolution model for lowtran 7," Tech. Rep. GL-TR-89-0122, Geophysics Laboratory, Air Force Systems Command, Hanscom AFB, MA.

Clodius, W. B., 1995: "Temperature Retrieval Algorithms Results Including Daytime Retrievals," LANL Memo NIS-1:**95-433**.

Cox, C. and W. Munk, 1954: "Measurement of the roughness of the sea surface from photographs of the sun's glitter," *J. Opt. Soc. Am.* **44**, pp. 838-850.

Henderson, B. G., J. Theiler, P. Villeneuve 1997, "The polarized emissivity of a wind-roughened sea surface: a Monte Carlo model," submitted to *Rem. Sens. Envir.*

Theiler, J., 1995: "Software for the MTI temperature retrieval pipeline," informal memorandum.

Theiler, J. and B. G. Henderson, 1997: "A Geometrical Constraint on Shadowing in Rough Surfaces," *Proc SPIE* **3122**, 271-279.

Tornow, C. and C. C. Borel 1994, "Multi-angular multi-spectral night-time water temperature retrieval," MTI Technical Report **MTI-94-001**.

Tornow, C., C. C. Borel, and B. J. Powers, 1994: "Robust water temperature retrieval using multi-spectral and multi-angular IR mesasurements," *Proc. IGARRS '94*, 441-443 (1994).

7. DETECTING BODIES OF WATER

John J. Szymanski and Christoph C. Borel

7.1 Introduction and Goal

Before water-temperature retrievals are performed it is necessary to identify pixels that are predominantly water and therefore produce a water map. Of course, a priori knowledge of water bodies from independent topographic information and/or previous MTI images will be used when available and deemed accurate. In the present conception of this algorithm, water maps are produced from the near-infrared band D (0.76 to 0.86 microns), which has a 5 m ground-sample distance (GSD), versus the 20 m GSD of the thermal infrared (TIR) bands. Two approaches will be outlined in this paper, one that involves active modeling of the atmosphere and water surface and another that requires more interaction and relies on a statistical sampling of surface reflectance. Both use the visible bands.

7.2 Scientific Basis

The reflectance of water in band D is very low, with a residual dependence on the level of "yellow gunk" (i.e., soil and other sediments) and chlorophyll (see Fig. 7-1). Band D is located just past the vegetative "red edge," and water is essentially black in this band. Other materials, such as asphalt, can also appear black in band D. So, it may prove necessary to use the green band (B) to sense the presence of chlorophyll and, therefore, differentiate other "black" pixels from water pixels. See Section 16 on water quality. One could also use the NDVI as a counter-indicator, *i.e.*, water has a low NDVI. Essentially, any of the VIS-NIR bands (A-D) will have low reflectance for water, with the possible exception of band B as noted above. Detailed evaluation of the algorithm performance will reveal the gains obtained using bands A-C, and these bands will be used in addition to band D where appropriate in the algorithm outlined below.

Wind speed, angle of incidence, and angle of detection all affect the reflectance of water. Also, atmospheric transmission and scattering affect the radiance detected in band D. Following Hamilton et al. (1993) and Carder et al. (1993), we can model the atmospheric transmission, angular, and atmospheric-scattering effects and derive the water-leaving radiance, L_w

$$L_w = \left(L_{TOA} - L_{path} - L_{sky}\rho\tau_{atm}\right)/\tau_{atm} \ , \qquad (7\text{-}1)$$

where L_{TOA} is the measured radiance at the top-of-the-atmosphere, L_{path} is the radiance scattered into MTI along the path, L_{sky} is the radiance looking up from the surface into space, ρ is the Fresnel reflectance of water, and τ_{atm} is atmospheric transmission. The last term represents the irradiance from the sky in a random direction that is reflected back into MTI. A MODTRAN simulation provides the needed atmospheric correction factors using atmospheric precipitable water as an input (as determined by the water vapor retrieval algorithm). Finally, the reflectance is determined by the relation

$$\text{Reflectance} = L_w / L_{inc},$$

where L_{inc} is the incident solar irradiance, corrected for atmospheric transmission.

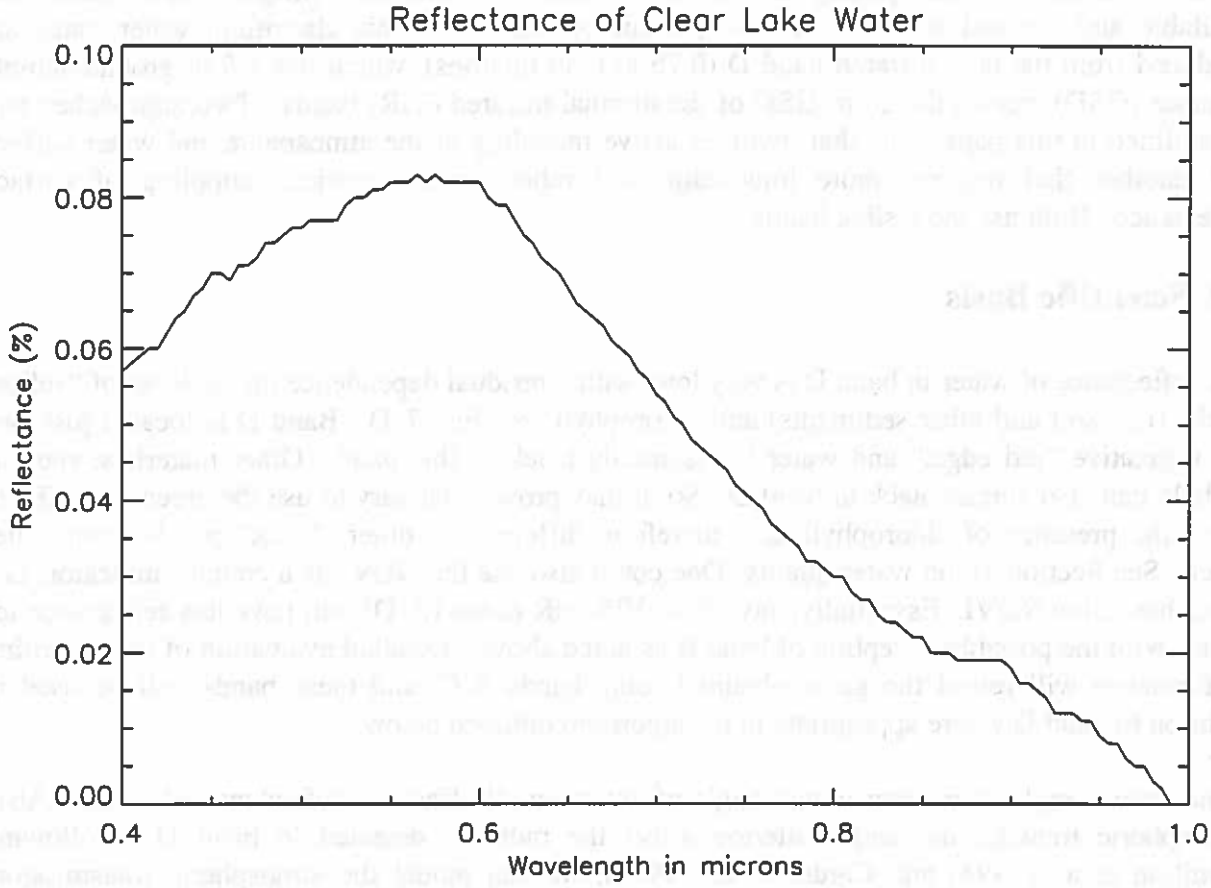

FIGURE 7-1. Reflectance for clean lake water. Note that in the region of Band D (0.76 to 0.86 microns) the reflectance is particularly low.

7.3 Algorithm Steps

A simple threshold applied to the atmosphere-corrected reflectance tags water pixels (with reflectance less than the threshold indicating water). If the wind speed is known, then the threshold can be modified with input from a wind-speed-dependent water reflectance model such as the Cox-Munk model (Cox and Munk, 1954). Different chlorophyll concentrations can also be added to 6S simulations of the water reflectance.

After the first-order water map is produced from band D (A-D), the low-resolution bands can be checked for consistency in the water-identified pixels. In other words, if a pixel is identified as being water, the VNIR and SWIR bands should have reflectances consistent with water.

The threshold can also be determined from the statistics of the scene itself by histogramming the band D reflectance or producing scatterplots of two VIS-NIR reflectances. Indeed, it may be possible to work with top-of-the atmosphere radiances, using a histogram to set the appropriate threshold to differentiate water pixels from the remainder of the scene. This approach would work if atmospheric corrections are similar across the scene, an assumption that is likely to be true for MTI images. This approach needs input from a data analyst to properly set the threshold by studying reflectance or radiance distributions. If available, independent topographic data can also guide the analyst in setting the threshold by identifying known water pixels.

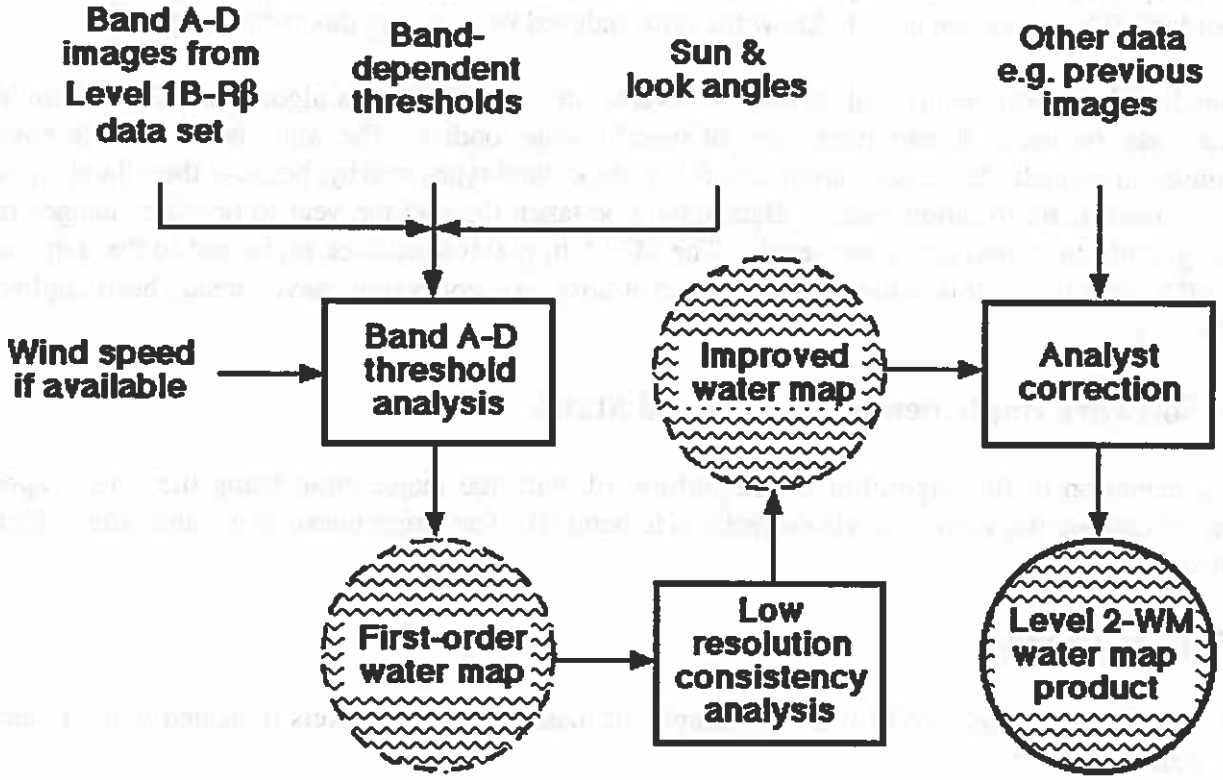

Figure 7-2. Water map generation algorithm.

One of the important tests of the efficacy of this algorithm is to study images and check for contiguity of water pixels. In other words, we should not have water bodies with many, isolated non-water pixels in them. By the same token, we don't expect many isolated water pixels surrounded by other (land) surface types. The contiguity test is best applied to test data from real sensors. A data analyst can also use the contiguity test to adjust the threshold.

7.4 Error Budget

To be researched further. Clearly, ground-truth data are relatively easy to obtain for various size and shape water bodies. Scenes with ground-truth measurements can then be compared to the MTI retrieval.

7.5 Validation Plan

We can test this algorithm by using synthetic earth-surface imagery. For example, water bodies of various shapes can be subjected to wind at several speeds and have varying levels of chlorophyll concentration. MODTRAN is used to produce simulated top-of-the-atmosphere radiances. The algorithm is then used to produce a water map, and a confusion matrix of assumed versus correct atmospheres can be constructed. Furthermore, a single threshold would be applied and the sensitivity with different wind speeds tested. Given that we often will not know the surface wind speed for MTI images, we need to know the error induced by guessing this incorrectly.

Ground-truth measurements will be used at several sites to validate this algorithm. Ground-truth, in this case, means high-resolution maps of specific water bodies. The water bodies should have examples of asphalt, dense vegetation, and other 'dark' land types nearby, because these land types are the most likely to mimic water. Data should be taken through the year to provide changes in algae growth, turbidity, and water levels. The MTI 5 m pixels should be registered to the maps at the ~0.3 pixel level. It is assumed that verified atmospheric corrections have already been applied to the data.

7.6 Software Implementation Plan and Status

Implementation of this algorithm is straightforward, with the major input being the water-vapor retrieval (and perhaps atmospheric corrections to band B). The larger question is validation, which is discussed above.

7.7 Data Product

The water mask, Level 2-WM will be a simple bit mask with water pixels indicated with '1' and non-water pixels '0'.

References:

Carder, K.L., P. Reinersman, R.F. Chen, F. Muller-Karger, C.O. Davis, and M.K. Hamilton, 1993: *Remote Sensing of Environment,* **44**, 205.

Cox, C. and W. Munk, 1954: *J. Opt. Soc. America*, **44**, 838.

Hamilton, M.K., C.O. Davis, W.J. Rhea, S.H. Pilorz, and K.L. Carder, 1993: *Remote Sensing of Environment*, **44**, 217.

8. SUBPIXEL TEMPERATURE RETRIEVAL

John J. Szymanski and Pawel Smolarkiewicz

8.1 Introduction and Goals

The multispectral information available from MTI can, under certain conditions, be used to measure more than one surface temperature in a single pixel. This information can be used in water-only pixels to pick out the edges of a thermal plume or, potentially, to retrieve water temperature for mixed land-water pixels. The latter is particularly useful for narrow water channels, where a significant portion of the water surface is contained in mixed land-water pixels (see Fig. 8-1).

8.2 Scientific Basis

Retrieving more than one temperature per pixel is a difficult task. Consider the general problem of surface temperature retrieval. The radiance measured at the top of the atmosphere (TOA) in MTI band i is

$$L^i_{TOA} = \varepsilon^i B^i(T_{surface})\tau^i_{atm} + L^i_{up} + L^i_{down}(1-\varepsilon^i)\tau^i_{atm}, \quad (8\text{-}1)$$

where ε^i is the emissivity in MTI band i, B^i is the Planck function averaged over band i, $T_{surface}$ is the surface temperature (our goal), τ_{atm} is the atmospheric transmission in band i, and the last two terms are the upwelling and reflected downwelling radiances in band i. The basic problem is that we have N measurements ($N = 5$ for the MTI thermal IR (TIR) channels), but we have at least $N+1$ unknowns (the 5 ε^i emissivities and one temperature, $T_{surface}$). This ignores the unknown upwelling and downwelling radiances and the unknown atmospheric state. In the case of a water temperature retrieval, we know the emissivities, and $T_{surface}$ can be robustly retrieved (see the sections on the robust and physics-based water-temperature retrievals). Furthermore, in a mixed pixel we in principle have $2(N+1)$ unknowns.

There are several additional pieces of information that we can use. For example, the nominal MTI image acquisition involves two looks at each scene (nadir and 60°). Information from these two looks can be used to eliminate some of the atmospheric effects. Also, day and night image acquisition allows one to look at the same scene under different thermal conditions (well into the night, the temperature contrast may reverse from its daytime bias, between materials with different emissivities). We also have the advantage with MTI of pixels taken in the visual range that have a 4x smaller ground-sample distance (5 m). This can be used to identify mixed land-water pixels a

priori. Thus, we can use the VNIR bands to measure the fractions of a mixed, 20 m GSD pixel that are different surface types (e.g., define a land-water boundary, as in the Detecting Water Bodies chapter).

Clearly this problem is difficult enough without considering more than two temperatures per pixel. Two cases can be considered:

1. Retrieving two temperatures from a pixel containing two materials with substantially different, but known, emissivities. The specific case of interest to MTI is a mixed land-water pixel.

2. Retrieving two temperatures from a pixel with a single material at two different temperatures (for example, a pixel that is homogenous in composition, but partially in shadow, or a thermal plume in water).

It is argued below that the first case is the easiest to retrieve temperatures (although far from 'easy').

8.3 Algorithm Steps and Modeling

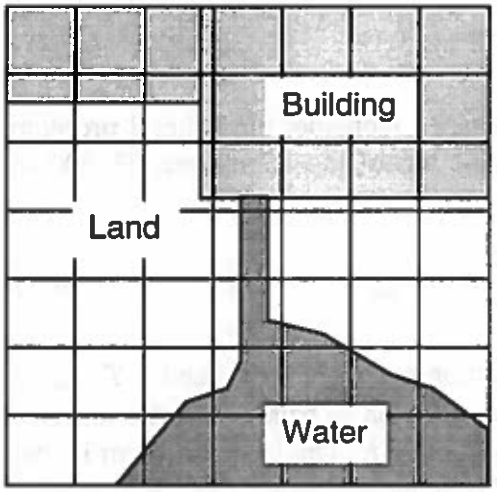

Figure 8-1. Pixels superimposed on a scene. Note the several types of mixed-pixels in the scene.

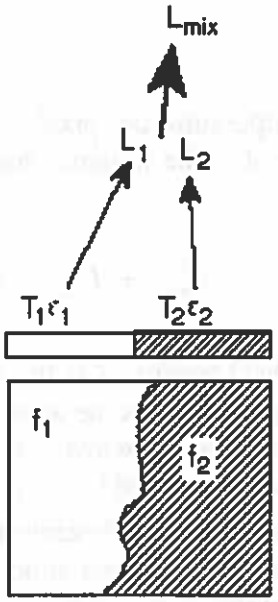

Figure 8-2. Definition of a mixed pixel.

Results

8.3.1 Retrieving temperatures from a mixed pixel

The top-of-the-atmosphere (TOA) radiance emitted by a mixed pixel in band *i* is (assuming the independent-pixel approximation, i.e., no coupling between the subpixels, which is a very good approximation in the TIR)

$$L^i_{mixed} = \left(f_1\varepsilon^i_1 B^i(T_1) + f_2\varepsilon^i_2 B^i(T_2)\right)\tau^i + L^i_{up} + L^i_{down}(r^i)\tau^i_{atm} \quad , \qquad (8\text{-}2)$$

where r^i is the reflectance of the mixed pixel, f_1 and f_2 are the areal fractions of the pixel that are at temperatures T_1 and T_2, respectively, τ^i_{atm} is the atmospheric transmission, the ε's are emissivities, and the B's are Planck functions (see Fig. 8-2). Reflected, downwelling radiance will be a small effect for high-emissivity natural surfaces and will be ignored here. If the emissivities are known and the fractions f_1 and f_2 can be determined from spatial cues in the visible or a priori knowledge entered by a data analyst, then we are left with 8 unknowns (upwelling radiance, 5 atmospheric transmissions and 2 temperatures) and the 5 TIR band measurements. Therefore, some atmospheric model is needed. Upwelling radiance and atmospheric transmission can be parameterized for the five TIR bands as a function of columnar water (CW) and effective atmospheric temperature T_{eff}(atm). A consistent set (i.e., a set that produces smooth temperature values) of *CW* and T_{eff}(atm) values can be produced using the physics-based temperature retrieval method described elsewhere. The physics-based temperature retrieval would be applied over a set of pixels that are believed to have a single, uniform temperature. Thus, if *CW* and T_{eff}(atm) are determined from an independent set of pixels, we are left with 5 measurements and 2 unknowns, the two temperatures. Further atmospheric information from the MTI two-look manuever would be used, if possible.

With the approximation outlined above, the measured radiance from a mixed pixel is

$$L^i_{mixed} = (f_1\varepsilon^i_1 B^i(T_1) + f_2\varepsilon^i_2 B^i(T_2))\tau^i_{atm}(CW) + B(T^{eff}_{atm})(1-\tau^i_{atm}(CW)). \quad (8\text{-}3)$$

In this model τ^i_{atm} is a function of columnar water (CW) and the second term has been substituted for the upwelling radiance. We use the *CW* and T_{eff}(atm) values from the physics-based temperature retrieval and define a new quantity

$$L^i_{reduced} = \left(L^i_{measured} - B(T^{eff}_{atm})(1-\tau^i_{atm}(CW))\right) \Big/ \tau^i_{atm}(CW) = \left(f_1\varepsilon^i_1 B^i(T_1) + f_2\varepsilon^i_2 B^i(T_2)\right), \quad (8\text{-}4)$$

which can be fit for T_1 and T_2, given some knowledge of the emissivities and the fractions f_1 and f_2. Note that the fit is easier if the two emissivities are not equal, provided they are known because there is more structure from band-to-band to separate the two terms in equation 8-4. The algorithm outlined here is illustrated in Fig. 8-3. It may be useful to introduce the concept of "virtual cold" developed by Gillespie et al. (1990) to further aid in the unmixing.

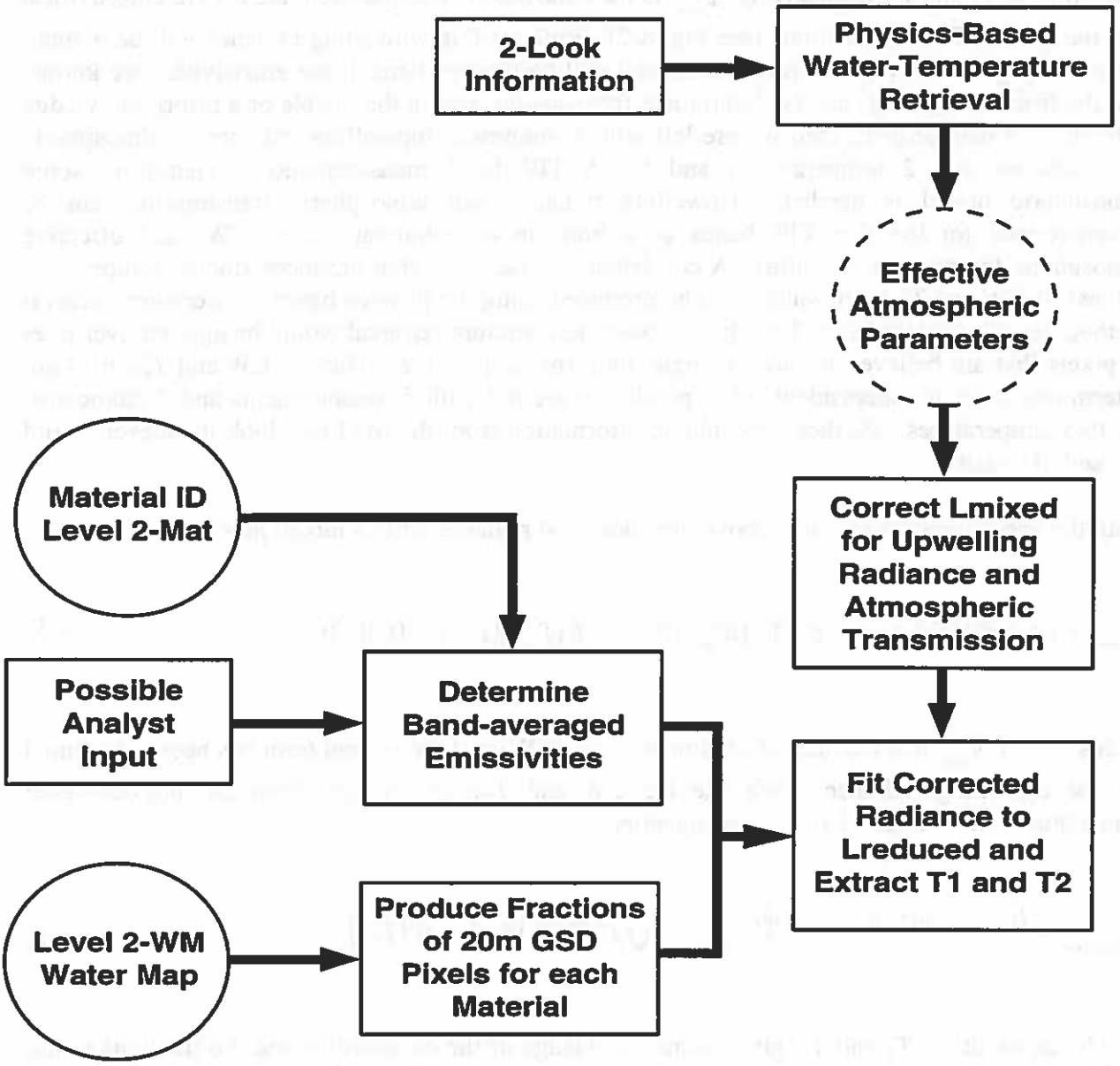

Figure 8-3. Subpixel temperature retrieval algorithm.

8.3.2 Modeling results

A synthetic river scene was created with riverbank pixels that are partly land and partly water. No atmospheric effects were included. The radiance from mixed pixels in the scene was modeled with equation 8-4 and smearing due to the detector noise and calibration errors was added. No emissivity or areal fraction errors were used. The retrieved rms water temperature error is ~2°K.

In the next model, errors in our knowledge of the emissivities are included by retrieving the temperature using the average emissivity of eight different soil types from the Salisbury (Salisbury and D'Aria, 1992) database. The TOA radiance from each pixel is simulated by randomly choosing among the eight soil types. The temperatures are retrieved using the average emissivity. A 3% rms error is assumed in the areal fractions, which is based on the fact that the water map will have 4x smaller GSD than the thermal bands and typically several of the smaller (5m) GSD pixels will be mixed land-water pixels. The resulting water-temperature rms error is ~2.5°K.

8.3.3 Other situations

What can be done in the other situation, where a pixel contains a single material that is at two different temperatures? Conceptually, one can consider extracting two temperatures in this situation, although the task is considerably tougher than in the first situation. The governing hypothesis in this report is that the radiance produced in the 5 MTI thermal bands from two Planck functions, L_{mixed} is distinguishable, within errors, from the radiance produced by a single Planck function (i.e., the radiance that would be produced by a single-temperature pixel). If these two situations can't be distinguished, then there is no chance of retrieving two separate temperatures. The extent to which this hypothesis is fulfilled sets the limits of the method.

It is instructive to study the radiance as a function of wavelength for two situations: (1) a mixed pixel whose radiance is described by two Planck functions at two temperatures and (2) a single Planck function representing the radiance one expects if the pixel were pure. The temperature used in the single Planck function is a straight average of the brightness temperatures in the 5 MTI TIR bands. To further accentuate the differences between pure and mixed pixels, take these ratios

$$R_{mixed} = L^{N}_{mixed} / L^{'}_{mixed} \qquad R_{pure} = L^{N}_{pure} / L^{'}_{pure} \tag{8-5}$$

Ultimately, the errors in R_{mixed} must be smaller than the difference

$$D = \left| 1 - \frac{R_{mixed}}{R_{pure}} \right| . \tag{8-6}$$

For $f_1 = f_2 = 0.5$, $T_1 = 300$K, and $T_2 = 280$K, $R_{mixed} = 23.3$, $R_{pure} = 24.3$, and D=4.4%.

Can $D = 4.4\%$ be detected with MTI? Assume the following SNRs for bands J - N, respectively: 200, 200, 500, 500, 500, and assume that the relative calibration of the MWIR and LWIR bands is 0.5%. In this case, the error on $R_{mixed} = 0.73\%$. Thus, a mixed pixel with two temperatures of 300 K and 280 K has an observable deviation from the radiances observed from a single Planck function. Note that no explicit reference has been made to water, or even that the emissivities be the same for the two subpixels, but it is assumed that the emissivities are known and uniform

within the pixel. With an error on R_{mixed} of 0.73%, and assuming at least 2 standard deviations from unity, a minimum temperature difference of 12K is observable (for $f_1 = f_2 = 0.5$).

8.4 Error Budget

This is not a retrieval as much as an analysis package, requiring substantial user input. Clearly, a few degree or smaller temperature error is desirable, but we may use this algorithm to set bounds given certain input parameter ranges.

8.5 Validation Plan

Validation of this algorithm requires two types of scenes:

1. A scene containing an artificial water channel with water temperature measurments and good knowledge of the relative locations of pixels and the edges of the channel (0.5 5 m (VIS) pixels would be sufficient).
2. A lake shore scene, again with good registration and water-temperature measurements.

The H.R. Robinson power-plant complex in South Carolina has both of these attributes. Water temperature measurements to 1°K are sufficiently accurate. Atmospheric water vapor profiles and aerosol column densities are needed with moderate resolution (no better than are necessary for the physics-based water-temperature retrieval). In addition, some characterization of the ground emissivity (to 0.01-0.02, if possible) is needed.

Validation of the case where one material is at two temperatures is not considered here, because the algorithm for dealing with this case is not well-developed.

8.6 Software Implementation Plan and Status

The existing algorithm has been written in IDL and operates on synthetic scenes. Application of the algorithm to test data emulating the MTI bands will commence in the near future.

8.7 Data Products

The subpixel temperature retrieval is a level 4 product, requiring substantial user input, applied to a limited, user-specified region of interest. The output of the subpixel analysis, Level 4-Subpix, is a series of images of the region of interest specifying land temperatures, water temperatures, chisquared distributions, etc. At present, the only situation that will be supported is mixed land-water pixels with known emissivities and areal fractions.

References:

Gillespie, A.R., M.O. Smith, J.B. Adams, and S.C. Willis, 1990: in proceedings of the TIMS workshop.

Salisbury, J. W. and D. M. D'Aria, 1992: "Emissivity of terrestrial materials in the 8-14 μm atmospheric window," *Remote Sens. Environ.*, **42**, 83-106.

9. POWER ESTIMATES FROM THERMAL IMAGERY ANALYSES

Alfred Garrett

9.1 Objective

The objective of this algorithm development effort is to use thermal imagery from a source such as MTI to produce power estimates for nuclear reactors, fossil-fueled power plants and for other industrial processes that discharge large amounts of waste heat to cooling lakes, rivers, estuaries or the ocean.

9.2 Scientific Basis

Waste heat discharged to a body of water in the environment will ultimately be dissipated by the combined effects of vertical and horizontal turbulent diffusion, transport by the mean flow, evaporation, convective heat loss and radiative cooling. It is a fairly straightforward process to simulate these heat dissipation processes with a 3-D hydrodynamic code that includes models that describe the energy exchanges between water and air. A complete set of inputs to such a simulation includes: meteorological data (wind speed and direction, air temperature, dewpoint temperature, cloud cover and pressure), water depths, outfall and inlet temperatures, Julian day, latitude, and in some cases tidal amplitudes and periods or river flow rates. Given these inputs, simulations can be performed with different power plant cooling water flow rates until a best fit is found between observed and simulated thermal images. If the hydrodynamic code plus the inputs produce an accurate simulation of reality, the cooling water flow rate corresponding to the best fit should be close to the actual flow rate. In most cases, cooling water inlet and outfall temperatures for the power plant can be taken directly from the calibrated thermal image. Given the temperature rise from inlet to outlet and the cooling water flow rate, the rate at which energy is being discharged to the environment can be calculated from:

$$P = CF\Delta T \qquad (9\text{-}1)$$

where P is power, C is a conversion constant, F is cooling water flow rate and ΔT is the temperature rise from inlet to outlet. Eq. (1) gives only the part of the power being produced that is discharged to the environment. If electrical power is being generated, the total power estimate must account for the generating efficiency, which is usually about 33% for nuclear power plants and about 38% for fossil-fueled power plants.

9.3 Algorithm Steps

1. Gather data needed to create input files for simulations: meteorological data, bathymetric data, cooling water inlet and outlet locations and if possible their depths, tidal amplitudes and periods, river flow rates.
2. Create input files and computational grids.
3. Run series of simulations with varying flow rates.
4. Compare simulated thermal images to observed thermal images using subjective and objective methods. Objective methods include standard statistical quantities such as correlation coefficient, RMSE (root-mean-square error) and bias, but the primary measure of agreement between observed and simulated thermal images is the Total Excess Energy (TEE), defined by:

$$TEE = \rho c_p \sum_{i=1}^{N} (T_i - T_a) \Delta x \Delta y \Delta z \qquad (9\text{-}2)$$

   In Eq. (9-2), ρ is density of water, c_p is specific heat of water, N is the number of nodes or corresponding pixel values in the observed image, T_i is the temperature at a computational node or corresponding pixel value, T_a is the ambient water temperature and $\Delta x \Delta y \Delta z$ are nodal spacings in the horizontal and vertical directions. Typically, only 3 simulations are needed to determine the cooling water flow rate which produces equal values of simulated and observed TEE.
5. Compute power from Eq. (9-1), and adjust to account for electrical power generation, if necessary.

9.4 Validation Plan

A 3-D hydrodynamic code (ALGE) with the characteristics described above was developed at the Savannah River Technology Center (SRTC) and has been tested with data taken in a cooling lake at the Savannah River Site (Garrett and Hayes, 1997). The ALGE code has also been verified with cooling lake data from a large commercial nuclear power plant (Garrett, 1995a, 1996a, 1996b). Additional verification work is now underway to determine the accuracy of power estimates derived from simulations by ALGE of waste heat discharged to the ocean by another commercial nuclear power plant. The work at the commercial nuclear sites is funded by other programs.

The initial verification work described above made use of thermal imagery from remote sensing systems that required ground truth data to calibrate the imagery. Garrett (1995b) showed that biases in the calibration of thermal imagery can produce large errors in the power estimates. A key part of ALGE verification for MTI will be assessment of the accuracy of the ALGE's power predictions using imagery calibrated with MTI's thermal retrieval algorithms, not ground truth. The water temperature that MTI and all other remote sensors measure is the "skin" temperature, which is the temperature of the uppermost millimeter of water. The skin temperature is typically

cooler than the bulk water temperature just below, because evaporative cooling removes heat from warm water faster than it can be replaced from below by thermal conductivity and diffusion. Evaporative cooling models such as those used by the ALGE code make use of empirical correlations based on bulk water temperature measurements, not skin temperatures. After MTI is launched, it will image on a continuous basis a power plant that discharges heated water to a cooling lake and a power plant that discharges to an estuary or river. The ground truth data collected at these sites will include both skin and bulk water temperatures. These data will be used to determine if existing methods to correct for skin-bulk water temperature differences are adequate (Schluessel et al, 1990).

The MTI verification data base for the ALGE code should contain at least 25 images taken over at least one year for each of the two power plant sites, along with collateral data such as meteorology. SRTC will use these data to determine the accuracy of ALGE's power estimates based on MTI's temperature retrieval algorithm, including corrections for differences between skin and bulk water temperatures.

9.5 Status

As stated above, SRTC has developed the ALGE code and some verification work has already been done. That verification work is continuing. SRTC is now selecting candidate power plants to be regularly imaged by MTI. SRTC is also determining what instrumentation will be needed for ground truth measurements at these sites.

References

Garrett, A. J., 1995a: "Power station thermal model validation for IR Toolkit Project." TCS-49590-95, Savannah River Technology Center, Aiken, SC. (TSC)

Garrett, A. J., 1995b: "Sensitivity of operating power estimates to biases in temperatures derived from thermal imagery." SRTC-NN-95-10, Savannah River Technology Center, Aiken, SC 29808.

Garrett, A. J., 1996a: "Power station thermal model validation for IR Toolkit Project. August 1995 Collection." TCS-49652-96, Savannah River Technology Center, Aiken, SC. (TSC)

Garrett, A. J., 1996b: "Power station thermal model validation for IR Toolkit Project. January 1996 Collection." TCS-001-96, Savannah River Technology Center, Aiken, SC. (TSC)

Garrett, A. J., and D. W. Hayes, 1997: "Cooling lake simulations compared to thermal imagery and dye tracers." *J. Hydr. Engrg.*, **123**(10), 885-894.

Schluessel, P., W. J. Emery, H. Grassl, and T. Mammen, 1990: "On the bulk-skin temperature difference and its impact on satellite remote sensing of sea surface temperature." *J. Geophys. Res.*, **95**(C8), 13341-13356.

10. ESTIMATION OF COOLING TOWER POWER

Lance O'Steen

10.1 Objective

The objective of this project is the development of a procedure utilizing MTI visible and IR imagery of cooling tower plumes, in conjunction with high-resolution, 3-D plume simulations, to estimate cooling tower power, and hence the operating power of the facility serviced by the cooling tower.

10.2 Scientific Basis

Power generating facilities must expel to the environment a certain percentage of their total energy production as waste heat. This is normally accomplished by the direct discharge of hot process water to a nearby body of water or by thermal exchange of the hot water stream with the atmosphere utilizing a cooling tower. Heat transfer in a cooling tower occurs by convection, due to a temperature difference between the water and air, and by latent heat effects, as water evaporates into the ambient air stream. Latent heat typically represents 80% of the total heat exchange in a cooling tower. Thus, a cooling tower operation often produces a cloud water plume, and the amount of water vapor available for condensation is largely determined by the operating power of the tower. A cloud water plume is a good scatterer of solar radiation and a strong infrared emitter. Thus both visible and IR imagery can potentially be used to obtain information on plume geometry and cloud properties related to radiative transfer within the plume. In principle, this information can be compared with plume simulation results to yield a power estimate. A schematic of a typical cooling tower operation is shown in Figure 10-1.

The operating power of a cooling tower is given by,

$$P = G\,(H_{out} - H_{in}) \qquad (10\text{-}1)$$

where: G = mass flow rate from the tower

H_{in} = enthalpy of the ambient air entering the bottom of the tower

H_{out} = enthalpy of the air exiting the top of the tower

The enthalpy terms in the above equation are dependent on the temperature and humidity of the associated air streams. The tower exit stream for a visible plume is saturated, and thus is a function of temperature only. If the ambient air temperature and humidity near the ground can be determined (tower inlet), then the cooling tower power is a function of exit flow rate and temperature. With sufficient spatial resolution it might be possible to directly measure the tower exit temperature from IR imagery. Unfortunately, MTI does not have sufficient resolution for this measurement. In any case, the flow rate would remain an unknown. Another approach is to compare imagery of the entire plume with simulations of the plume and attempt to iteratively (varying exit temperature and velocity) determine the power level. Actual plume geometry can be examined with either visible or IR imagery through MTI's dual look capability, while the spatial distribution of the above plume properties allows the calculation of IR emission and transfer within the plume (scattering can be included if necessary) for direct comparison with MTI imagery.

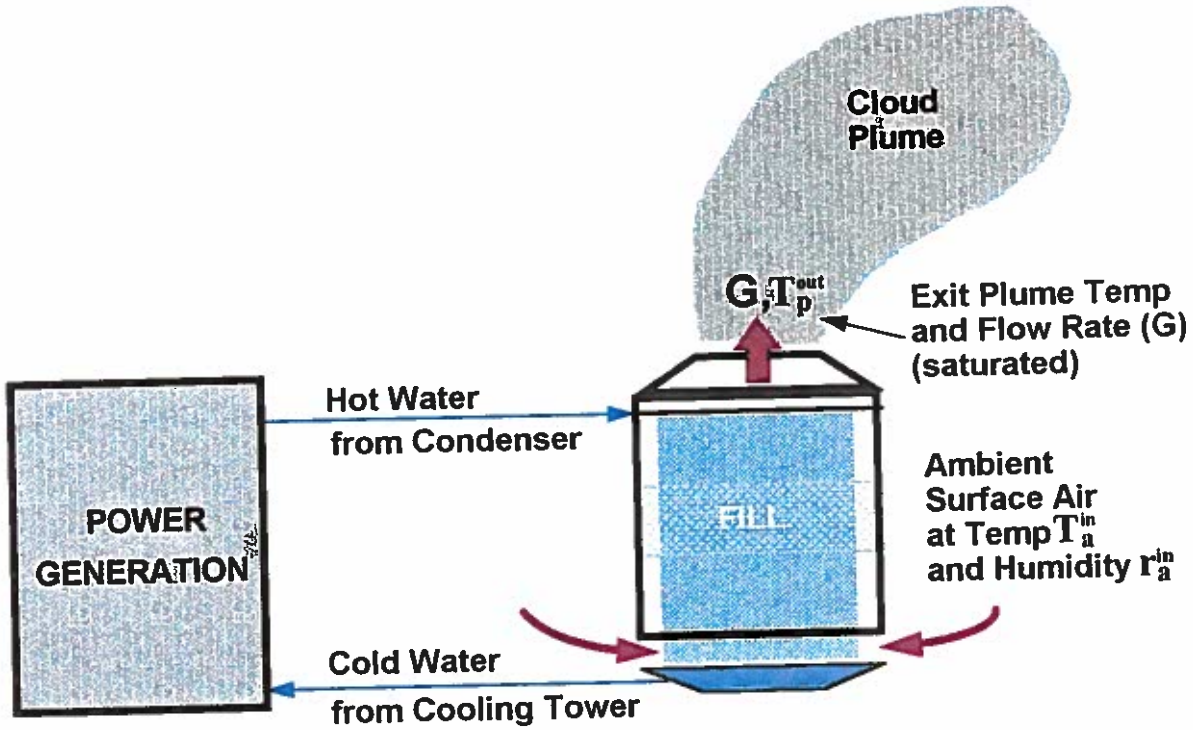

Figure 10-1: Schematic of typical cooling tower operation.

Any type of plume simulation will require as input: (1) the tower exit temperature and velocity, and (2) ambient temperature, humidity and wind from the ground to the top of the plume. Simulation output should include realistic plume geometry and the spatial distribution of cloud water, temperature and drop size within the plume. This will necessitate the use of a high resolution, 3-D plume simulation. The Regional Atmospheric Modeling System (RAMS) developed at Colorado State (Pielke, et al., 1992) is used for this simulation task. RAMS is a 3-D, nonhydrostatic boundary-layer model developed primarily for simulating mesoscale circulations. However, RAMS has been used for large-eddy simulations (Walko, et al., 1992) and high-resolution flow around simple structures (Nichols, et al., 1993). Plume simulations generated with RAMS indicate that total cloud water volume is a strong function of power, with $\Delta V/\Delta P$ ranging from 1400 to 2700 m^3/MW for fixed ambient meteorology (O'Steen, 1996). A typical power for these simulations was 2400 MW, with a plume volume of 2.6×10^6 m^3. In the same simulations, variations in plume volume due to turbulent motions were found to be relatively small with $\sigma_v/V < 0.1$. Simulation studies were also performed to determine the sensitivity of plume volume to variations in ambient temperature and humidity at constant power, since errors in the estimation of ambient meteorology are inevitable. Simulation results suggest that $\Delta V/\Delta T$ and $\Delta V/\Delta q$ are about 0.3×10^6 m^3/K and 1.3×10^6 m^3/g/kg, when the ambient temperature (T) and specific humidity (q) are relatively constant over the height of the plume. Nominal values of ambient temperature and humidity were 287 K and 4.9 g/kg for these meteorological sensitivity studies. In Figure 10-2, cloud water volume versus tower power is plotted for a simulation with fixed meteorology. Two additional points are plotted for which the ambient, plume-level temperature and specific humidity were perturbed. For the high humidity simulation, the specific humidity was increased from 4.9 to 5.1 g/kg; the temperature was lowered 3 K for the low temperature simulation.

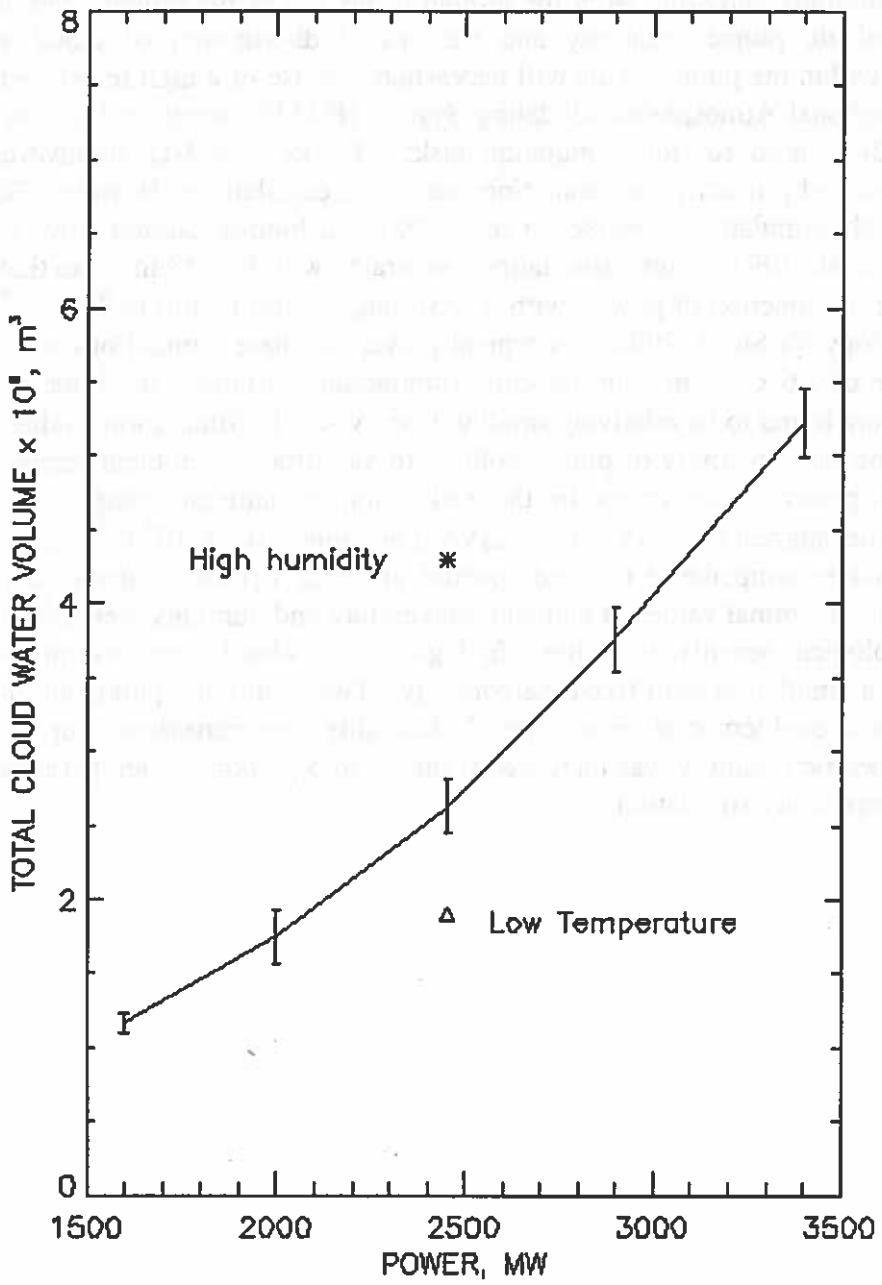

Figure 10-2: Cloud water volume versus tower power for a simulation with fixed meteorology.

Thus typical errors in the thermodynamic structure of the atmosphere cannot be ignored when estimating power from measurements of plume volume. In the simulations to date, the boundary-layer atmospheric model used to generate the cooling tower plume (RAMS) was also used to generate the ambient meteorology. This is done at a resolution sufficient to capture any local surface induced effects (e.g. drainage flows), with the model initiated at least 12 hours prior to the tower simulation. Large-scale model results, sounding data and surface data are all used to initialize

the boundary-layer model. In addition, MTI-derived air temperatures, from ground vegetation and tree top foliage, can be assimilated into the boundary-layer simulation and used directly in the power calculation. MTI water vapor column information might also provide a check on the simulation results. In areas of complex terrain and limited data, the use of a mesoscale model can be essential in obtaining accurate meteorology (Fast and O'Steen, 1992). If errors in the ambient meteorology are not significantly biased, then a set of collections/simulations should be able to eliminate most of the power estimation error due to errors in meteorology.

As discussed above, for a given meteorological profile, the plume volume and cooling tower power are functions of tower exit velocity and temperature. However, these functional relationships are not the same, and therefore the tower velocities and temperatures which produce a specific plume volume do not generally correspond to a constant power level. Fortunately, tower design velocities for both forced (8 to 12 m/s) and natural draft towers (3 to 6 m/s) do not vary widely, thus this power error should be less than 25%. Plume radiance calculations in the IR might be able to narrow this error even further. A two-stream radiative transfer code based on Mie theory has been developed for this calculation.

10.3 Computational Algorithm for Cooling Tower Power Estimation

To minimize meteorological errors in the power estimate, the following steps should be performed for a series of collections:

(1) Estimate a vertical profile for ambient meteorology using a boundary-layer model and all available model data (large scale), upper air data, surface data, and MTI derived data. Use comparison of model results with observations in the region to determine if significant bias exits in the model predictions.

(2) Calculate plume volume from MTI imagery at two view angles. Also use solar plume shadow to provide a third "view angle" for volume estimation if visible imagery is being utilized.

(3) Use data from (1) and specified values of tower exit velocity and temperature to simulate cloud water plumes. Determine values of velocity and temperature which produce observed plume volume for a reasonable range in tower velocity.

(4) Calculate the cooling tower power for the velocities and temperatures found in (3).

(5) If IR imagery is being utilized, calculate plume radiance and compare with imagery. Use this information to narrow the power range found in (4).

10.4 Verification of Power Estimation Algorithm

The power estimation procedure outlined above will initially be verified through a series of ground-based field studies of a pair of large natural draft cooling towers at the Plant Vogtle generating station near Augusta, Georgia. The cloud water plumes will be photographed (both visible and IR)

from several different angles and the volume estimated from the images. The algorithm for this volume estimation has been developed and tested. Daily operating power for the towers will be provided by Vogtle personnel. Ambient meteorological data will be collected from nearby towers operated by the DOE's Savannah River Site. One of these towers provides wind and temperature information to a height of 300 meters; tower height is 175 m. Humidity is available to 60 meters. It is also anticipated that upper air data will be available during the collections from airsonde launches at the Savannah River Site. After MTI is launched, Vogtle will be the primary candidate for space-based verification studies, although an alternate site is possible. The space-based verification will be similar to the ground studies, with intensive meteorological data collection during fly-overs and simultaneous ground-based imagery collection. In addition, cooling tower exit temperature and velocity will be continuously monitored. It is also anticipated that cloud water content and drop size will be measured to provide a more direct verification of the plume simulation.

10.5 Project Status

Code development for the ground-based verification project is complete and ground based verification studies will begin in early 1998. Further code development and testing will be required for volume estimation based on MTI imagery. Additional radiation code development will also be required to include plume-to-satellite radiative transfer (atmospheric effects).

References

Pielke, R.A., W.R. Cotton, R.L. Walko, C.J. Tremback, W.A. Lyons, L.D. Grasso, M.E. Nichols, M.D. Moran, D.A. Wesley, T.J. Lee, and J.H. Copeland. "A Comprehensive Meteorological Modeling System – RAMS", *Meteorology and Atmospheric Physics*, **49**, 69 (1992).

Nichols, M.E., R.A. Pielke and R. Meroney. "Large Eddy Simulation of Microburst Winds Flowing Around a Building," *J. Wind Eng. and Ind. Aero.*, **46** & **47**, 229 (1993).

Walko, R.L., W.R. Cotton and R.A. Pielke. "Large-Eddy Simulations of the Effects of Hilly Terrain on the Convective Boundary Layer", *Boundary-Layer Meteorology*, **58** (1-2), 133, 1992.

Fast, J.D., and B.L. O'Steen. "Use of the 1991 ASCOT Field Study Data in a Mesoscale Model Employing a 4-Dimensional Data Assimilation Technique", Sixth Conference on Mountain Meteorology, Portland, OR, Sept. 29 - Oct. 2, 1992, p. 249-255, American Meteorological Society.

O'Steen, B.L. "Cooling Tower Plume Simulation with a Mesoscale Model", SRTC Technical Report, SRTC-NN-95-28.

11. CLOUD MASKS

Anthony B. Davis

11.1 Introduction and Goal

Clouds are defined in this report —on purely optical grounds— as highly reflective/emissive regions in the atmosphere and —apart from the occasional dust storm, forest fire, or volcanic eruption— this definition translates directly into the usual definition of a cloud as a concentration of liquid-water droplets and/or ice crystals. These are indeed the scattering particles that produce the phenomenon of "cloud" readily observable to the naked-eye. Clouds can form anywhere from the ground (a dense fog) to the upper troposphere (cirrus) with horizontal extensions ranging from tens of meters ("puffs") to thousands of km (marine stratocumulus decks). Even under this slightly restrictive optical definition, clouds are a frequent occurrence: likely 1/4 to 1/3 of the Earth is shrouded in cloud at any given time. The climatological number for cloud-cover is somewhat larger but includes cases optically thinner than we care to consider here.

Under the not-too-grazing-incidence-or-viewing conditions that apply generically to MTI scenes, "highly reflective/emissive" invariably means "optically thick;" some authors extend the notion of "cloud" to optically thin layers such as sub-visible cirrus, which we treat in another report (Section 12 on Thin Cirrus Detection/Removal). The implicit assumption here is that any occurrence of liquid or solid H_2O in the atmosphere defines a cloud. It must be emphasized that such semi- to quasi-transparent "clouds" are, for all practical purposes, comparable to aerosol layers in the remote-sensing context. Both aerosol, a boundary-layer phenomenon, and optically thin "clouds," typically high-altitude cirrus, are atmospheric perturbations of a remotely-sensed signal otherwise dominated by surface features and, as such, should be corrected for (cf. Sections. 12 & 13).

The goal of the algorithm described in this report is to detect the presence of clouds in an MTI scene and, if necessary, separate them from "clear sky" portions of the scene. Thus defining a cloud "mask," a product that informs us about how clear the sky is between satellite and ground for a given pixel. In the MODIS cloud mask [Wharton and Myers, 1997], a "degree" or "probability" of cloudiness is assigned to each pixel, cf. Fig. 2. Because of the much higher spatial resolution of MTI (5–20 m vs. 0.25–1.0 km for MODIS), this will not be necessary: a pixel is cloudy or not.

It must be realized however that clouds affect the measured pixel value even if they do not occur along the direct line-of-sight, especially in VIS/NIR channels. First, pixels can have measurable radiances —although lower than "normal"— coming from surface points that are in the geometrical shadow of a cloud. This is witness to the fact that there is a diffuse as well as a direct component to local surface irradiance. As diffuse reflectors, isolated clouds can "channel" or